Available online at www.sciencedirect.com
ScienceDirect
Comput. Methods Appl. Mech. Engrg. 384 (2021) 113892
Computer methods in applied mechanics and engineering
www.elsevier.com/locate/cma

Machine learning augmented reduced-order models for FFR-prediction

Fredrik E. Fossan[a,*], Lucas O. Müller[b], Jacob Sturdy[a], Anders T. Bråten[c,d], Arve Jørgensen[c,e], Rune Wiseth[c,d], Leif R. Hellevik[a]

[a] *Department of structural Engineering, Norwegian University of Science and Technology, Norway*
[b] *Department of Mathematics, University of Trento, Italy*
[c] *Clinic of Cardiology, St. Olavs Hospital, Norway*
[d] *Department of Circulation and Medical Imaging, Norwegian University of Science and Technology, Norway*
[e] *Department of Radiology and Nuclear Medicine, St. Olavs Hospital, Norway*

Received 24 August 2020; received in revised form 23 April 2021; accepted 24 April 2021
Available online 31 May 2021

Graphical Abstract

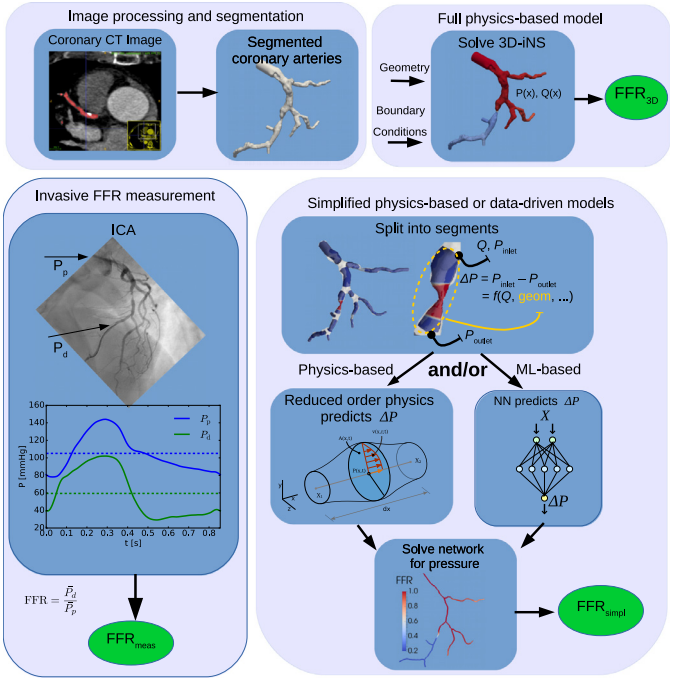

Abstract

Computational predictions in cardiovascular medicine have largely relied on explicit models derived from physical and physiological principles. Recently, the application of artificial intelligence in cardiovascular medicine has grown substantially.

* Corresponding author.
E-mail address: fredrik.e.fossan@ntnu.no (F.E. Fossan).

https://doi.org/10.1016/j.cma.2021.113892

However, successful application of purely data-driven methods requires a sufficiently large and rich dataset. An alternative to purely data-driven methods is to incorporate prior physics-based knowledge into the learning process to reduce the amount and quality of data necessary for a performant model. We analyzed the benefit of this alternative for prediction of pressure and flow in pathological coronary arteries. We trained fully-connected feed forward neural networks (NN) to predict pressure losses in coronary arteries. The training and test data were obtained by solving the 3D incompressible Navier–Stokes (3D iNS) equations. The coronary flow and various geometrical data were used as inputs to train a purely data-driven NN. We investigated two methods for incorporation of prior physics-based knowledge from a reduced-order model (ROM) into NNs that predicted pressure losses across stenotic and healthy coronary segments. First, we trained NNs to predict the discrepancy between the ROM and 3D iNS pressure loss. Second, we augmented the data by including the ROM pressure loss prediction as an input feature to a NN that predicted 3D iNS pressure. Both approaches for incorporation of prior knowledge from the ROM significantly improved prediction of pressure losses across healthy and stenotic segments relative to the purely data-driven approach, especially for lower amounts of data. The incorporation of NN predictions of coronary segment pressure losses in a coronary network model resulted in Fractional Flow Reserve (FFR) predictions with error standard deviation of 0.021 with respect to 3D iNS FFR. In comparison, the standard deviation of repeated FFR measurements is 0.018.

Keywords: Computational FFR; Physics-informed neural networks; Reduced-order modeling

1. Introduction

Physical principles have long been applied to study physiology, and advancements in mathematical and computational models have led to continued growth in related research over the past few decades. This has culminated in the application of physics-based computational models in the clinic, such as for diagnosis of obstructive coronary artery disease (CAD) [1]. More recently, artificial intelligence and machine learning techniques have gained popularity, and their application may result in a paradigm shift in cardiovascular medicine [2]. Machine learning techniques have shown great utility in cardiovascular imaging [3,4] and risk assessment [5,6]. Machine learning enables a data-driven approach that can infer outputs of interest directly from minimally processed data (with the limitations of biases present in the algorithm and chosen datasets). Data-driven approaches are, however, dependent on the quality and representation of the data available for training. Importantly, machine learning algorithms perform poorly or fail to generalize when trained on insufficient data. In addition, predictions from purely data-driven approaches may violate physical principles as well as regulatory requirements [7].

The limitations of data-driven approaches motivate the incorporation of prior knowledge into the learning process to improve generalization and constrain the problem [7]. For example, Raissi et al. [8] employed automatic differentiation to neural networks (NNs) to add an additional term to the loss function that penalized violation of governing laws of physics. Other efforts have incorporated prior knowledge through addition of physics-based computer simulations to the input dataset [9–12]. These prior efforts demonstrate that combining physics-based knowledge with data-driven machine learning approaches might offer the best of both worlds, particularly in cases with sparse data [11,13]. In this work we explore various approaches for prediction of pressure losses in coronary arteries based on pure physics, pure machine learning, and combinations that include prior physics-based information in the learning process.

Fractional Flow Reserve (FFR) is the gold standard for diagnosis of intermediate stenoses in patients with chronic coronary artery disease [14]. FFR is measured during invasive coronary angiography (see the left part of Fig. 1) by insertion of a catheter with a pressure sensor and is calculated as the ratio between the cardiac cycle averaged pressure distal and proximal to the stenosis

$$\mathrm{FFR} = \frac{P_d}{P_p},$$

where P_p is normally measured at the ostium, *i.e.* where the coronary tree branches off the aorta. If FFR is below 0.8 the stenosis is considered hemodynamically significant, and it is generally recommended to intervene by percutaneous coronary intervention. If FFR is above 0.8 optimal medical therapy alone is recommended. Despite the European Society of Cardiology's recommendation to use FFR to guide revascularization in chronic CAD patients [14], FFR remains underused due to associated costs, its invasive nature, and the need for trained interventionalists [15].

The underuse of invasive FFR in clinical practice has motivated research towards noninvasive prediction of FFR. Most early attempts for non-invasive FFR prediction relied on solving the incompressible 3D Navier–Stokes equations (3D iNS) in segmented coronary arteries [16–18]. This approach requires minimal assumptions about the physical behavior of blood flow. However, clinical applicability requires fast and accurate prediction, which limits the applicability of full 3D models, the use of which is difficult to automate since they require additional pre/post-processing steps and have considerably higher computational cost with respect to simpler models.

Recent research to improve clinical applicability of noninvasive FFR prediction has focused on developing simpler and faster models based on; (1) reduced-order physics such as 1D blood flow or lumped parameter models [19–22], and (2) purely data-driven approaches [23–27].

In this work, we propose a hybrid approach to integrate reduced-order physics-based models with data-driven models for prediction of pressure losses in the context of computational FFR prediction. First, segmented coronary arteries are split into stenotic and healthy segments by applying a Gaussian filtering procedure. Next, NNs are trained to reproduce the pressure losses predicted by 3D iNS across the segments. We consider a purely data-driven approach which only include the flow and various geometrical data as inputs. Further, we consider two approaches of informing NNs with prior physics-based knowledge: (1) training NNs to predict the discrepancy between 3DiNS pressure loss and pressure loss predicted by idealized reduced-order models (ROM) and (2) including the ROM pressure loss as a feature. Subsequently, we incorporate trained NNs into a FFR prediction-pipeline.

We compare segment pressure losses and FFR predicted by the purely data-driven NN model and the physics-informed NN models with those obtained with the 3D iNS model. We repeat these comparisons for NNs trained on three different dataset sizes to investigate if informing the NNs with physics-based knowledge reduces the required dataset size to achieve a given accuracy. Finally, we compare all considered approaches for FFR prediction, with invasive FFR measurements. To the best of our knowledge such a comparison between a purely data-driven approach, a purely physics-based approach and physics informed data-driven approaches for prediction of pressure loss and FFR has not been done. Fig. 1 illustrates how FFR is measured in the clinic as well as providing a graphical overview of the different modeling approaches for noninvasive FFR prediction compared in the study.

2. Methods

2.1. Data collection and processing

We collected data from 64 patients with stable coronary artery disease and a clinical indication for invasive investigation with FFR due to significant coronary artery disease diagnosed with coronary CT angiography (CCTA). The patients were included in an ongoing clinical trial at St. Olavs hospital, Trondheim, Norway [28]. Furthermore, 26 patients were recruited retrospectively. Positive FFR prevalence (FFR $\leq$ 0.8) was 40 % and 22% in the prospectively and retrospectively recruited populations, respectively. We present here only a brief description of the data collection and study procedures, as a more detailed description of recruitment criteria, exclusion criteria, and procedure protocols has been reported previously [29].

Recruitment. All patients included in this study underwent CCTA, which found at least one clinically significant stenosis, and were further referred to Invasive Coronary Angiography and FFR measurement.

Vessel segmentation and computational domain meshing. For each patient both the left and the right coronary trees were segmented. All patients were segmented with ITK-SNAP [30], while for 28 patients additional independent segmentations were performed with Mimics (Materialise's Interactive Medical Image Control System; Materialise, Leuven, Belgium). The coronary arteries were segmented until their presence was difficult to distinguish from background tissue, corresponding to a radius of $\sim$ 1 mm.

Surface mesh processing, addition of flow extensions and 3D meshing was performed using the open-source library Vascular Modeling ToolKit (VMTK) [31,32]. The meshing refinement level was determined by a radius-adaptive meshing algorithm parameter called edge-length factor l_f, which was set to $l_f = 0.21$ for all simulations. Thus the total number of elements varied per case, ranging from $\sim$1 to $\sim$5 million. A mesh independence study showed that such discretization provided mesh independent FFR predictions for a set of 4 patient-specific geometries. The 3D volume meshes formed the basis for both the reference 3D iNS model, the ROM, the purely data-driven NN model and physics-informed NN models.

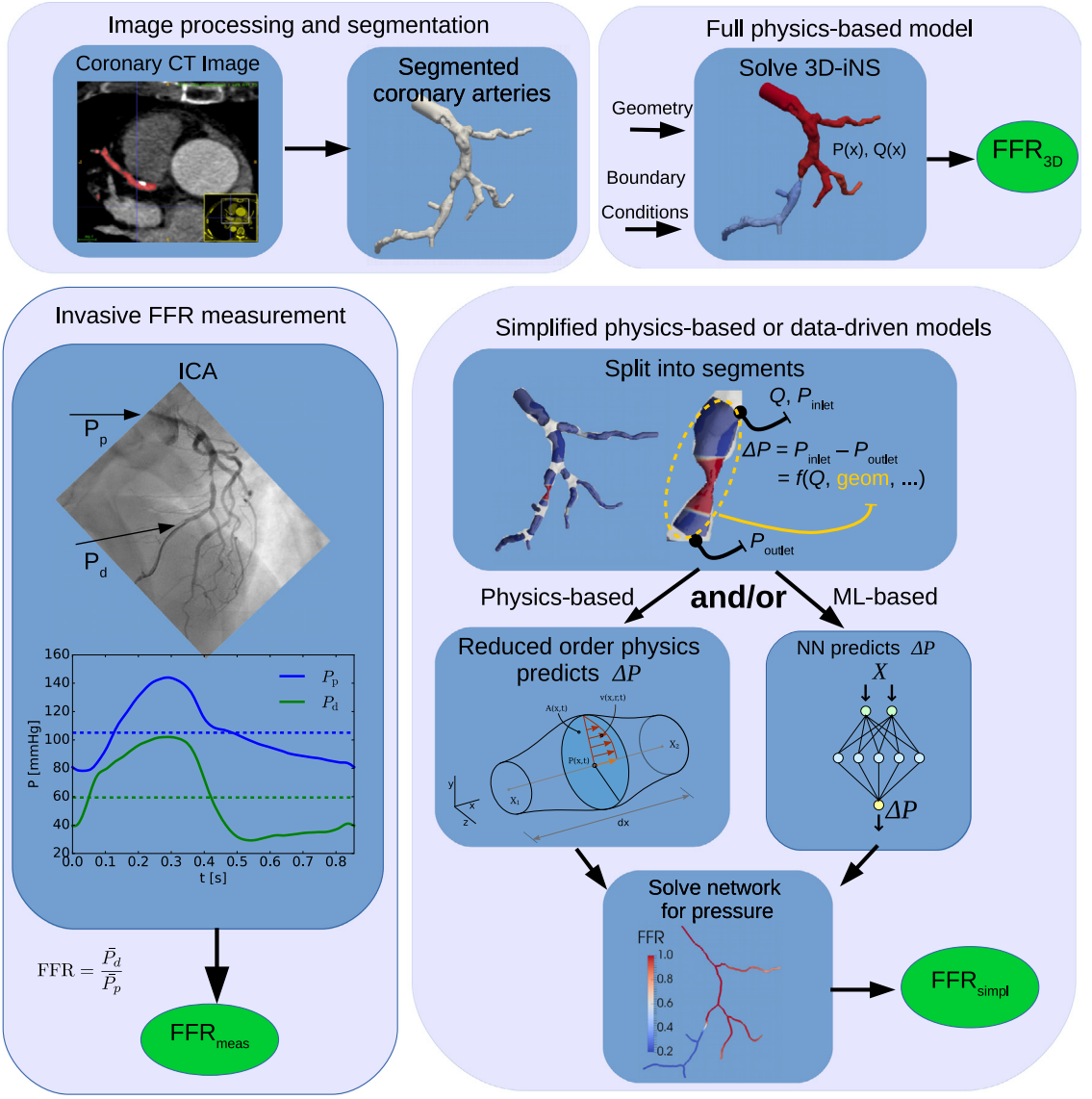

Fig. 1. Illustration of FFR measurement obtained during invasive coronary angiography (ICA) and overview of the non-invasive approaches for prediction of FFR used in this study. For the non-invasive methods, the coronary geometry was segmented from CT images (top). Simulations based on the 3D incompressible Navier–Stokes equation were run to yield pressure and flow in the 3D domain, from which non-invasive FFR_{3D} was calculated (top right). Processing of the 3D domain was performed to split the domain into different segments, which formed the basis for the simplified models considered in this work (bottom right). The pressure loss across the different segments was predicted by (1) reduced-order physics and/or (2) by neural networks. Individual pressure losses along the different segments were incorporated into a coronary network model to yield pressure distribution in the coronary domain, from which non-invasive FFR_{simpl} was calculated.

The 3D volume mesh was used without additional processing for the reference 3D iNS model, however, for the remaining approaches the volume mesh was processed further. Centerlines were extracted from the 3D domain [32], and cross-sectional areas were calculated at an average spacing of 0.125 mm and used to calculate the radius, r, of an equivalent axi-symmetric cross-section. The centerlines were split into individual arteries (separated by junctions) using VMTK [22,32], and further split into stenotic and healthy segments. Healthy reconstructions of each artery's radius were estimated based on a Gaussian kernel filtering procedure [33]. Stenotic segments were automatically detected based on the deviation between the actual and reconstructed radii. The length of the stenotic segments was

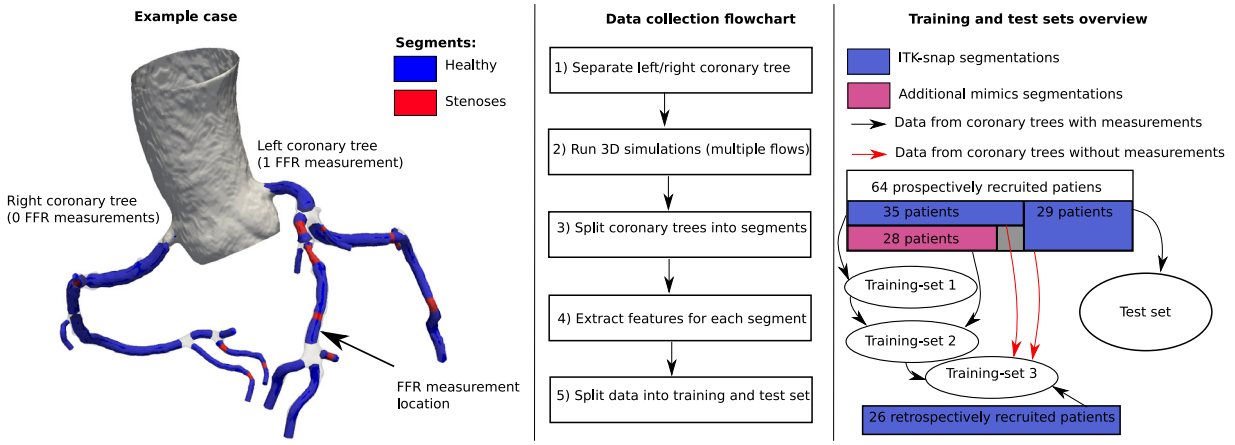

Fig. 2. Left: example patient, depicting the left and right coronary trees, which is split into arteries (separated by bifurcations in opaque), in addition to detected stenotic (red) and healthy segments (blue). A single FFR measurement was performed for this patient, indicated by the arrow. Middle: flowchart indicating the steps performed to collect data used for training NNs. Right: Overview of the origin of the test data in addition to the three training set sizes considered. (For interpretation of the references to color in this figure legend, the reader is referred to the web version of this article.)

automatically calculated based on a threshold for the similarity of the actual and reconstructed radii, in addition to a threshold based on the spatial variation of the radius. The left part of Fig. 2 shows an example patient where junctions are shown as semi-transparent regions, stenoses are depicted as red areas, while blue portions correspond to healthy segments. See [22,29] for further details related to the classification of segments as healthy or stenotic.

2.2. Non-invasive FFR prediction-pipeline

All approaches for non-invasive FFR prediction (3D iNS approach, ROM approach, data-driven NN approach and physics informed NN approaches) considered in this study shared a common data flow from clinical data to predicted FFR which was introduced by Müller et al. [29]. These predictions were made in two stages: first a baseline state of resting coronary hemodynamics was predicted from non-invasive clinical measurements. Second, the hyperemic state was predicted based on the distribution of pressure and flow in the baseline state. These two stages are necessary to model the drug induced dilation of peripheral coronary arteries that is required to invasively measure FFR.

The FFR prediction-pipeline may be summarized as follows:

1. Prediction of a baseline coronary state with prescribed inlet pressure and prescribed outlet flows.
2. Computation of resistances:

$$R^{\text{bln}}_{\text{out},l} = \frac{P^{\text{bln}}_{\text{out},l} - P_v}{Q^{\text{bln}}_{\text{out},l}}, \quad \text{with } l = 1, \ldots, N_{\text{out}}, \tag{1}$$

   where $P^{\text{bln}}_{\text{out},l}$ and $Q^{\text{bln}}_{\text{out},l}$ are the baseline pressure and flow at the lth of a total of N_{out} outlets. These values were extracted from the simulation results from the previous step. P_v is a reference venous pressure, which was set to $P_v = 5$ mmHg throughout this work.
3. prediction of a hyperemic state with prescribed inlet pressure and prescribed resistances at outlets. Such resistances were computed as

$$R^{\text{hyp}}_{\text{out},l} = \frac{R^{\text{bln}}_{\text{out},l}}{\text{TCRI}}, \quad \text{with } l = 1, \ldots, N_{\text{out}}, \tag{2}$$

where Total Coronary Resistance index (TCRI) is the factor by which peripheral coronary resistance drops from its value at baseline condition to its value in hyperemia. In this work we have used TCRI = 4 [34].

In both the baseline and hyperemic states, the inlet pressure was based on non-invasive cuff measurements. For further details on the pipeline and estimation of outlet flows, see [29]. For a given coronary tree, several sets of outlet flows were considered, resulting in a database of simulation results, as described in Section 2.3.1. Prediction of the hyperemic pressure (point 3. above) was used to estimate FFR non-invasively.

2.3. Reference 3DiNS approach

The steady state 3D iNS simulations treated segmented coronary arteries as rigid domains. Pressure was prescribed at the inlet boundary-condition and either flows (via prescribed parabolic velocity profiles) or resistance models were used at the outlet boundaries. A no-slip condition was assumed between the interface between the vessel walls and the blood. Laminar flow and an incompressible Newtonian fluid were assumed and the simulations were performed with FEniCS using CBCFLOW [35,36]. See [29] for further details related to the 3D iNS framework.

2.3.1. 3DiNS simulation database

We sought to develop a simplified approach for prediction of FFR with the aim to match the predicted 3D iNS CFD pressure losses as accurately as possible by means of simplified and computationally cheaper models. The NN models were thus trained to predict the pressure drop that the 3D iNS model predicted for a given segment and inflow.

For each coronary tree considered in this study, 3D iNS simulations with a number of different flow conditions were performed. The different flow conditions were obtained by applying different ways to prescribe outlet coronary flows in the FFR-pipeline described in Section 2.2. For each patient, total coronary flow was estimated as a fraction of cardiac output, which in turn was derived from patient-specific ultrasound measurements. Then, different flow distribution methods – distal Murray (DM), proximal Murray (PM) and transluminal attenuation gradient (TAG) – were used to distribute flow to each outlet, as described in [29]. In addition, a version of the vessel length flow distribution method proposed in [37] was used. This resulted in a dataset containing several hyperemic and baseline simulations of pressure and flow for each coronary tree, each corresponding to a flow distribution method. The number of available simulations per coronary tree was not the same. The most extensive number (10), of simulations were available for coronary trees with FFR measurements in the prospectively recruited patients. This database of simulations was available from a previous study [29]. In addition the database was augmented with simulations performed on newly available volume meshes from independent segmentations of a subset of coronary trees, coronary trees without FFR measurements, and coronary trees in retrospectively recruited patients (see Section 2.5.2 and Fig. 2). The number of simulations per coronary tree was lower for these cases (average number: 6).

For NN training and evaluation, a dataset was formed where each row corresponds to a particular healthy or stenotic segment of a particular coronary tree subjected to a specific flow and pressure state, as illustrated in Fig. 3. The coronary flow and various geometric measures formed the set of input features as described later in Section 2.5.1. The pressure drop across the segment was used as the training output.

2.4. Reduced-order model approach

In the ROM, a steady state 1D-axisymmetric model was used to predict pressure losses across healthy segments (ΔP_h):

$$\Delta P_\mathrm{h} = Q \int_0^l \frac{2\left(\zeta+2\right)\pi\mu}{A\left(x\right)^2}\mathrm{d}x + \frac{\rho}{2}\left(\frac{1}{A_\mathrm{out}^2} - \frac{1}{A_\mathrm{in}^2}\right) Q^2, \tag{3}$$

where μ and ρ are the viscosity and density of blood respectively, and ζ is a velocity profile parameter set to 4.31 based on results from a comparison of 1D and 3D theory in healthy coronary arteries [22]. Furthermore, l is the segment's length, Q is the flow across the segment, $A\left(x\right)$ is the spatially varying cross-section and A_in and A_out are the cross-sectional areas at the inlet and outlet of the segment, respectively.

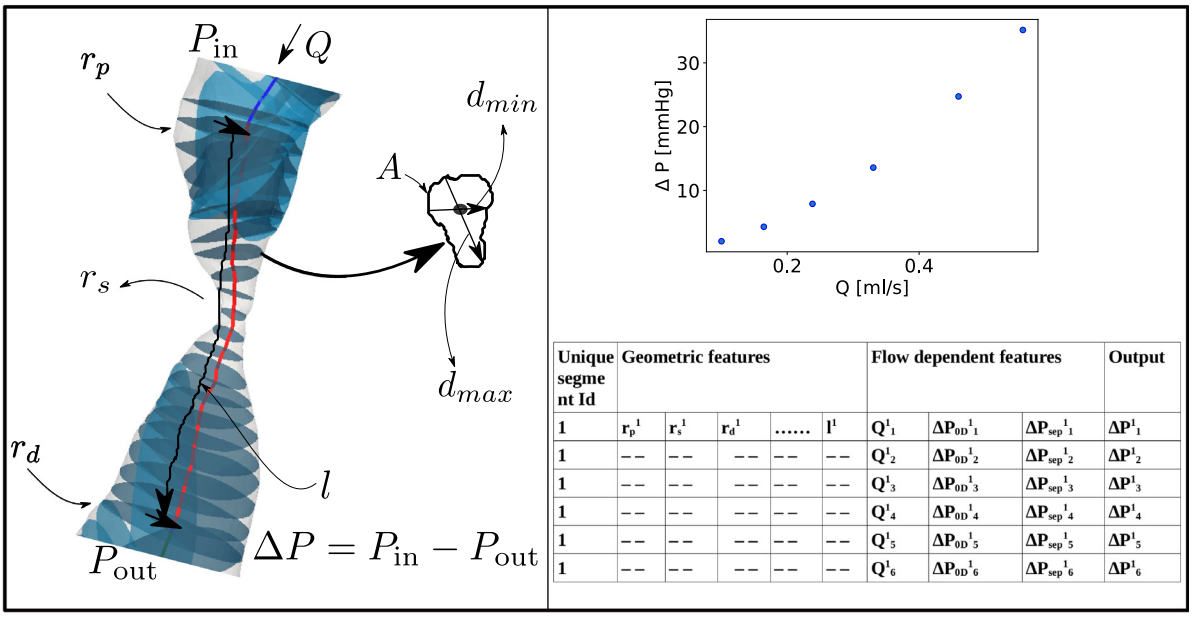

Unique segment Id	Geometric features					Flow dependent features			Output
1	r_p^1	r_s^1	r_d^1	.....	l^1	Q^1_1	$\Delta P_{0D}{}^1_1$	$\Delta P_{sep}{}^1_1$	ΔP^1_1
1	--	--	--	--	--	Q^1_2	$\Delta P_{0D}{}^1_2$	$\Delta P_{sep}{}^1_2$	ΔP^1_2
1	--	--	--	--	--	Q^1_3	$\Delta P_{0D}{}^1_3$	$\Delta P_{sep}{}^1_3$	ΔP^1_3
1	--	--	--	--	--	Q^1_4	$\Delta P_{0D}{}^1_4$	$\Delta P_{sep}{}^1_4$	ΔP^1_4
1	--	--	--	--	--	Q^1_5	$\Delta P_{0D}{}^1_5$	$\Delta P_{sep}{}^1_5$	ΔP^1_5
1	--	--	--	--	--	Q^1_6	$\Delta P_{0D}{}^1_6$	$\Delta P_{sep}{}^1_6$	ΔP^1_6

Fig. 3. Illustration of the extraction of relevant features for a specific stenotic segment (left), pressure drop (ΔP) for different flows (Q) across the segment (top right), and schematic of how the data for this specific segment is included as row-entries in a database containing many such segments (bottom right). The values were extracted from the 3D domain and 3D iNS solutions. The centerline of the artery is visible (blue/red line). The red part corresponds to the stenotic segment, which is also highlighted by the black line. Relevant features include the flow into the domain (Q), proximal radius (r_p), minimum radius (r_s), distal radius (r_d) and length (l). Radius values were based on extracting data from cross-sections as indicated, which were also used to extract minimum (d_{min}) and maximum (d_{max}) diameter values for each cross-section. (For interpretation of the references to color in this figure legend, the reader is referred to the web version of this article.)

The assumptions related to 1D theory of blood flow do not hold in stenotic segments. A modified version of the 1D model which includes an additional term related to flow separation, was applied to predict pressure loss at stenotic segments (ΔP_{s}):

$$\Delta P_{\text{s}} = Q \int_0^l \frac{8\,\pi\,\mu}{A^2} \mathrm{d}x \; + \frac{K_t \rho}{2\,A_0^2} \left(\frac{A_0}{A_s} - 1 \right)^2 \; Q^2, \tag{4}$$

where A_0 and A_s refer to the reference (average of inlet and outlet) and minimal cross-sectional areas of the stenotic segment respectively. Further, $K_t = 1.52$ is an empirical coefficient [38]. Note that the expression for the viscous part in Eq. (4) is different from that in [29] and originally proposed in [38]. In contrast to the original formulation, which includes experimentally motivated viscous and flow separation terms, the viscous part in the current form represented by Eq. (4), is physically motivated (Poiseuille flow), and is more in line with 3D theory in coronary arteries according to a recent study [39]. The integral terms in Eqs. (3) and (4) were solved numerically using the trapezoidal rule, with the integrands being evaluated at points with average spacing of 0.125 mm (corresponding to the centerline-points). Finally, conservation of total pressure was imposed as a coupling condition between connected arteries.

2.5. Purely data-driven NN and physics-informed NN models

Neural Networks are extremely powerful as they can in principle learn any relationship between arbitrary input and output data (assuming all relevant features are included). However, the amount of data required to adequately train a NN may be prohibitive. Further, complex NNs may generalize poorly when the training data only partially represents the range of possible inputs and outputs. We sought to investigate if incorporation of information from physically motivated models may improve the performance and training of NNs.

First, we trained NNs to predict ΔP_{3D} directly without incorporation of physics-based, reduced-order model information. Next, we trained NNs to predict the discrepancy between the pressure losses predicted by the reduced-order model and 3D iNS:

$$\epsilon_{\Delta P} = \Delta P_{3D} - \Delta P_{0D}\,, \tag{5}$$

where ΔP_{0D} refers to the reduced-order model's prediction of pressure loss, and is introduced as a common term to refer to either ΔP_h or ΔP_s depending on whether the predictions were made for pressure loss across healthy or stenotic segments respectively. Resulting NNs for prediction of pressure loss can thus be formulated as:

$$\Delta P_{\mathrm{NN},\Delta P}\left(X\right) = f_{\Delta P}\left(X\right)\,, \tag{6a}$$
$$\Delta P_{\mathrm{NN},\epsilon_{\Delta P}}\left(X\right) = \Delta P_{0D} + f_{\epsilon_{\Delta P}}\left(X\right)\,, \tag{6b}$$

where f represents the functional form of the neural networks and X is the vector of input features (to be defined). Additionally, we applied an alternative method to include physics-based knowledge by augmenting the input features, X, with the reduced-order model's prediction of pressure loss. We thus generated two additional approaches for predicting pressure losses across segments:

$$\Delta P_{\mathrm{NN},\Delta P}\left(X^{0D}\right) = f_{\Delta P}\left(X^{0D}\right)\,, \tag{7a}$$
$$\Delta P_{\mathrm{NN},\epsilon_{\Delta P}}\left(X^{0D}\right) = \Delta P_{0D} + f_{\epsilon_{\Delta P}}\left(X^{0D}\right)\,, \tag{7b}$$

where the superscript 0D in X^{0D} indicates that ΔP_{0D} (*i.e.* ΔP_h or ΔP_s) was included in the feature set.

2.5.1. Input features

The neural networks were trained using the following sets of input features:

$$X_1 = \left[r_p, r_d, r_s, l, Q\right]\,, \tag{8a}$$
$$X_2 = \left[r_p, r_d, r_s, l, Q, PCA_{r,1}, PCA_{ec,1}, r_{\mathrm{min,min}}\right]\,, \tag{8b}$$
$$X_3 = \left[r_p, r_d, r_s, l, Q, PCA_{r,1}, PCA_{ec,1}, r_{\mathrm{min,min}}, \Delta P_{\mathrm{sep}}\right]\,, \tag{8c}$$
$$X_1^{0D} = \left[r_p, r_d, r_s, l, Q, \Delta P_{0D}\right]\,, \tag{8d}$$
$$X_2^{0D} = \left[r_p, r_d, r_s, l, Q, PCA_{r,1}, PCA_{ec,1}, r_{\mathrm{min,min}}, \Delta P_{0D}\right]\,, \tag{8e}$$
$$X_3^{0D} = \left[r_p, r_d, r_s, l, Q, PCA_{r,1}, PCA_{ec,1}, r_{\mathrm{min,min}}, \Delta P_{\mathrm{sep}}, \Delta P_{0D}\right], \tag{8f}$$

where r_p, r_d, r_s are the proximal, distal and minimum segment radius, respectively, and l is the length of the segment. Moreover, VMTK was used to extract the cross-sectional area (A), minimum diameter (d_{min}), and maximum diameter (d_{max}) of each cross-section. These were further used to calculate the average ($r = \sqrt{A/\pi}$), minimum ($r_{\mathrm{min}} = d_{\mathrm{min}}/2$) and maximum ($r_{\mathrm{max}} = d_{\mathrm{max}}/2$) radius values corresponding to each centerline point. In relation to this, $r_{\mathrm{min,min}}$ represents the minimum observed minimum radius. For each segment, the radius data was re-sampled with equidistant spacing using 100 points for which the eccentricity ($r_{\mathrm{min}}/r_{\mathrm{max}}$) was also computed. Based on re-sampled data, a principal component analysis [40] was performed on both the eccentricity and equivalent radius to reduce the input data by using only the largest component for each variable (i.e. $PCA_{r,1}$, $PCA_{ec,1}$). Fig. 3 illustrates the extraction of geometrical features. See Appendix A.4 for a more detailed description of the principal component analysis. Finally, in an effort to incorporate dynamic and flow separation changes/losses on upstream pressure, ΔP_{sep} was calculated as the sum of the Bernoulli term in the healthy segments ($\frac{\rho}{2}\left\{\frac{1}{A_{\mathrm{out}}^2} - \frac{1}{A_{\mathrm{in}}^2}\right\} Q^2$) and the separation term in the stenotic segments ($\frac{K_t\rho}{2\,A_0^2}\left\{\frac{A_0}{A_s} - 1\right\}^2 Q^2$)[1] over a region 1 cm upstream of the beginning of the segment. We note that feature-set X_3 was not evaluated for the purely data-driven NN approach, since ΔP_{sep} is physically motivated.

[1] We note that the value for K_t was set to 2.2 in this term (while K_t was set to 1.52 in the evaluation of ΔP_s as noted earlier). We experimented with values 1.52 and 2.2, however, final hyper-parameter searches were run with $K_t = 2.2$ for this input-feature and (to not have to run lengthy hyper-parameter searches again) were thus used in the presented results.

2.5.2. Training, testing and validation sets

We split the data into a training set and a test set. Importantly, the test set was not used during the training process. The test set was composed of data from coronary trees with FFR measurement from the last 29 prospectively recruited patients. For each patient, data from either the left, right or both coronary trees were included depending on the location of invasive FFR-measurement(s). *e.g.* if invasive FFR was only measured in the left coronary tree, only data (from healthy/stenotic segments) in the left tree was included. The presented results are based on evaluation of models on the test set unless stated otherwise. While the same test set was used throughout this work we considered three different training set sizes in order to assess whether the dependence on dataset size differed between purely data-driven NN and physics-informed NN models. The three training sets are illustrated in Fig. 2 and described below:

In **Training set 1**, only data from 3D iNS simulations from one set of segmentations from the first 35 prospectively recruited patients were included. Moreover, only data from coronary trees which had FFR measurement was included.

In **Training set 2**, additional data from the 28 first prospectively recruited patients who had independent segmentations (Mimics) were included in the training set. Previous studies have showed that the uncertainty in coronary geometry is one of the main sources of errors in predicted FFR [22,29]. We compared FFR predicted by 3D iNS for the distinct segmentations and found a similar variation as reported in prior studies of the impact of geometric uncertainty on FFR prediction. As such these segmentations provide a meaningful level of independent training data as the variations in geometry are sufficient to change the resulting FFR; however, the additional information is likely less than would be added from a completely independent case from a new patient.

In **Training set 3**, additional data (to training set 2) from the retrospectively recruited patients was added. Furthermore, flow and pressure data from coronary trees without FFR measurements from the 64 prospectively recruited patients was also included.

2.5.3. Hyperparameters and learning

We trained fully connected feed forward neural networks to predict pressure ($f_{\Delta P}(X)$) or pressure discrepancy ($f_{\epsilon_{\Delta P}}(X)$) functions. Neural network training and evaluation was performed using the high-level neural network API Keras [41] to interact with TensorFlow machine learning implementations [42]. The TensorFlow optimizer Adam [43] was used to minimize the mean absolute error (MAE) of the difference between pressure or pressure discrepancy function:

$$\mathrm{MAE}_{\Delta P} = \frac{1}{n}\sum_{j=1}^{n}\left|\Delta P_{3\mathrm{D}\,j} - f_{\Delta P}\left(X_j\right)\right| \tag{9a}$$

$$\mathrm{MAE}_{\epsilon_{\Delta P}} = \frac{1}{n}\sum_{j=1}^{n}\left|\epsilon_{\Delta P\,j} - f_{\epsilon_{\Delta P}}\left(X_j\right)\right| \tag{9b}$$

Learning was performed using mini-batches and the maximum number of epochs was set to 20 000. In an effort to avoid over-fitting, we split the training set into a validation set and a learning set [44]. The learning set was used by an optimizer [43] to fit the NN's parameters, and after each epoch the performance of the NN was evaluated on the validation set. If the loss-function value was smaller relative to all previous epochs, the NN was saved as the "best" NN. Moreover, if the validation loss did not improve for the last 5000 epochs, the optimization was terminated (even if the maximum number of epochs, 20 000, was not reached).

For all approaches and training set sizes considered in this work, the validation set consisted of 25% of the segments in the training data, and the split of the training data into a learning and validation set was performed by random sub-sampling. The random sub-sampling was performed 10 times (*i.e.* for each approach the training procedure was repeated 10 times), in order to evaluate the sensitivity to the learning/validation split.

We performed hyper-parameter searches for the different approaches considered in this study to determine a set of parameters used to train for pressure loss/discrepancy across stenotic and healthy segments. This was used to define the number of hidden layers, number of neuron in each layer, the activation function in the hidden layers, in addition to the learning rate, l_1 regularization term and batch size. Such parameters are listed in Table 1.

Table 1
Hyperparameters for neural networks for prediction of pressure and pressure discrepancy across stenotic and healthy segments. Number of hidden layers (nHl), number of neurons per layer (N_n), activation function (act. func.), l_1 regularization term (reg. term) and mini batch size.

Segment type	Act. func.	nHl	N_n	L. rate	Reg. term	Batch size
Stenotic	ReLu	2	50	0.018	0.0004	291
Healthy	ReLu	2	54	0.016	0.0004	315

2.6. Evaluation of predictive performance

The performance of each simplified approach for prediction of pressure losses across segments was assessed by a number of statistics based on the difference $\delta_i = \Delta P_{3D} - \Delta P_{simpl}$. Here, i indexes the segments in the dataset and ΔP_{simpl} refers to predictions based on the ROM, the purely data-driven NN or informed NNs respectively. We considered the bias, standard deviation (std. error), mean absolute error, mean squared error (MSE), and R^2 score of ΔP_{simpl} vs. ΔP_{3D}. In addition we wanted to test the performance when excluding "outliers" in the dataset and thus computed the mean absolute error when only considering 90% of the test data (excluding the 10% highest pressure losses). For all NN approaches and for all dataset sizes and input feature sets considered, 10 different NNs were trained (corresponding to the 10 random learning/validation splits). Error metrics were computed for all the 10 NNs and the values reported here represent the mean and standard deviation of such error metrics.

We integrated the prediction of pressure losses across segments from the simplified approaches into a coronary network model (see Fig. 1). We then applied the FFR pipeline described in Section 2.2 to predict FFR_{simpl} and corresponding 3D iNS FFR predictions (FFR_{3D}) for the 29 patients in the test set. In these patients 50 invasive FFR measurements were performed, and the locations of these measurements determined the point of comparison between FFR_{simpl} and FFR_{3D}. In order to assess the performance in a range of flow/pressure states, three different flow distribution methods were considered, hence a total of 150 FFR predictions formed the basis for this comparison.

We note that the training of the individual NN models for prediction of pressure losses across segments was performed by using the 3D iNS flow as an input feature (in addition to any other features). However when the NN models were incorporated into the coronary network model, pressure and flow distribution in the coronary tree results from the non-linear interaction of pressure losses across segments, junctions and boundary-conditions. As such the flow, in addition to other dependent input features (ΔP_s, ΔP_h and ΔP_{sep}) were based on the distribution of flow obtained by solution of the non-linear problem. The nonlinear problem was solved in an iterative manner, and the above mentioned input features were recalculated for each iteration. For more details regarding the numerical treatment related to the coronary network model the reader is referred to [22,29].

We evaluated the performance of FFR_{simpl} vs. FFR_{3D} based on the bias, standard deviation, and mean absolute error based on the quantity $FFR_{3D} - FFR_{simpl}$. Furthermore, accuracy, sensitivity and specificity were calculated based on dichotomized data ($FFR_{3D} \leq 0.8$). For the NN approaches, error metrics resulting from the 10 trained NNs (corresponding to the 10 random training splits) were computed and the values reported here represent the mean and standard deviation of such error metrics.

Following the comparison with 3D iNS FFR predictions, we also evaluated the performance of FFR_{simpl} and FFR_{3D} for predicting the 50 invasive FFR measurements. In this comparison a single flow distribution method was considered, namely the best performing method according to the study by Müller et al. [29]. Error metrics were calculated in an equivalent manner as described above, however with invasive FFR used as reference.

3. Results

3.1. Training data

Tables 2 and 3 show an overview of the number of stenotic and healthy coronary artery segments in addition to the total number of pressure and flow pairs in the test set and in the three different training dataset sizes considered in this study. In addition average, standard deviation and the 10th, 25th, 50th, 75th and 90th percentiles for proximal radius, minimum radius, distal radius, length, flow and pressure are given.

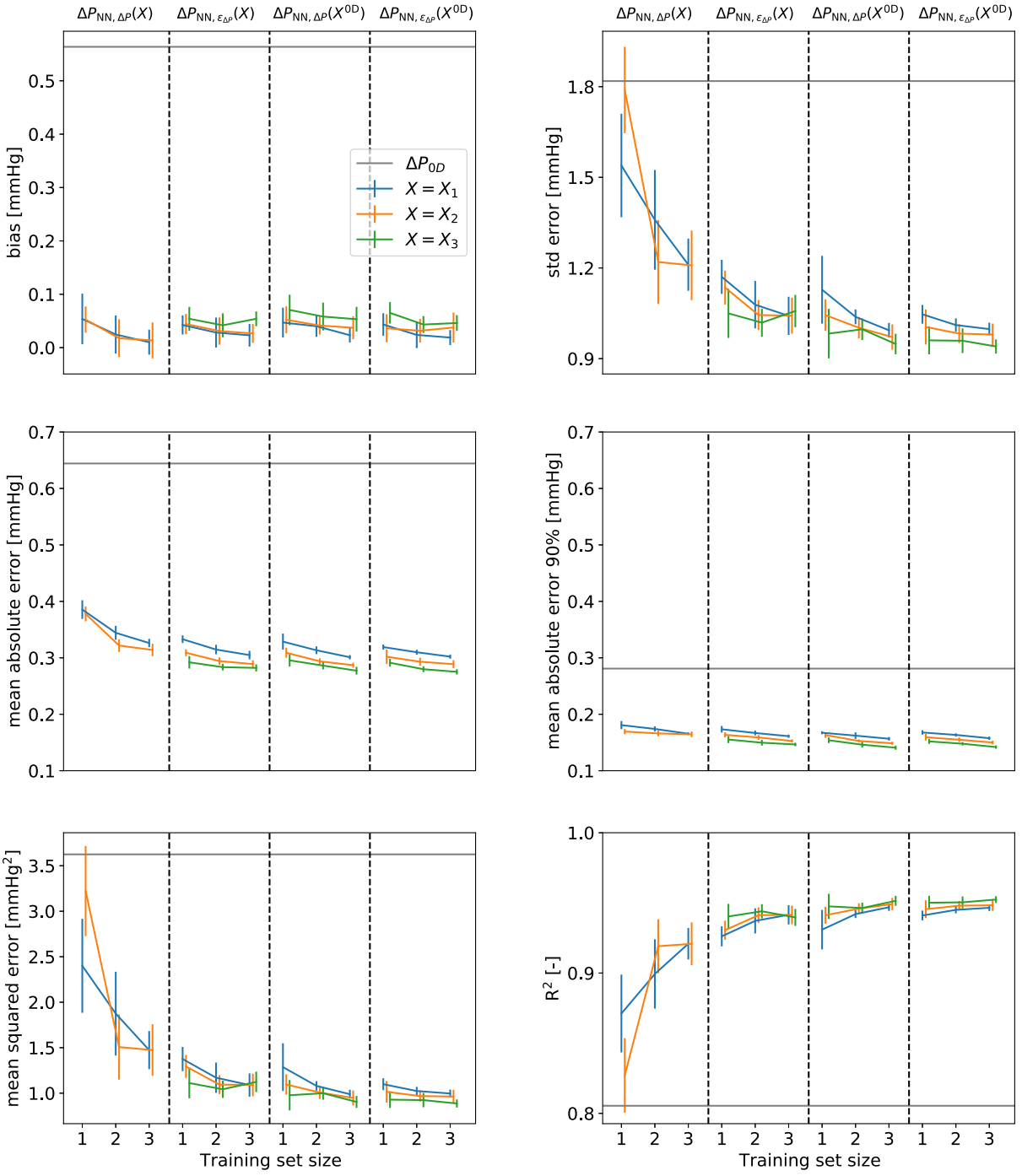

Fig. 4. Results for machine learning approaches for prediction of pressure losses across stenotic segments. The values presented by each line are the average of the metric across the 10 random training splits, while the vertical lines represent the standard deviation of the metric across the training splits. The bias, standard deviation, mean squared error, mean absolute error and mean average error considering 90% of the data, were calculated based on the quantity $\Delta P_{3D} - \Delta P_{\mathrm{simpl}}$, where $\Delta P_{\mathrm{simpl}}$ represent predictions based on the ROM or NN approaches. Similarly R^2 was calculated based on $\Delta P_{\mathrm{simpl}}$ vs. P_{3D}. See Table 5 in the Appendix for corresponding numerical values. (For interpretation of the references to color in this figure legend, the reader is referred to the web version of this article.)

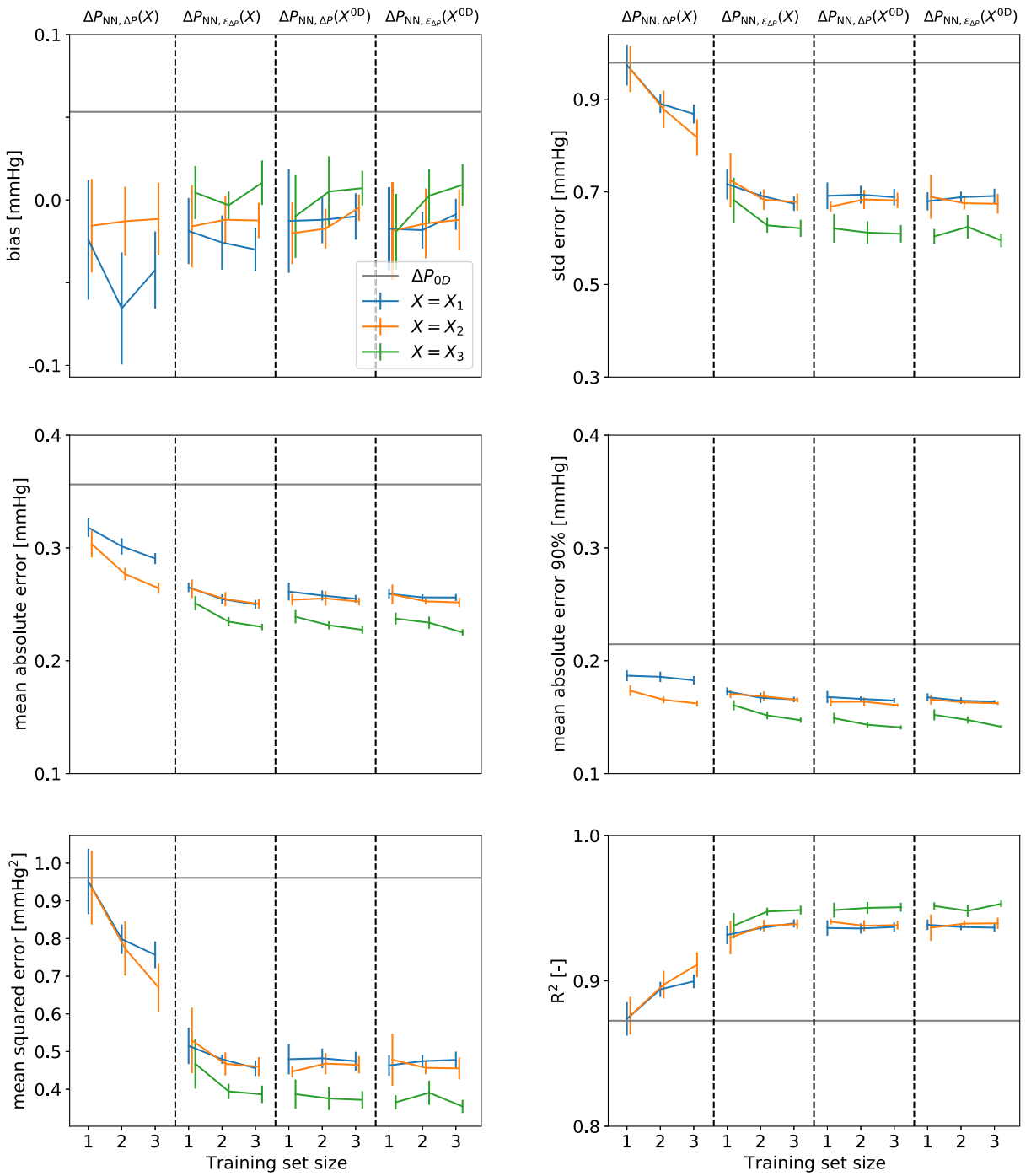

Fig. 5. Results for machine learning approaches for predicting pressure losses across healthy segments. The values presented by each line are the average of the metric across the 10 random training splits, while the vertical lines represent the standard deviation of the metric across the training splits. The bias, standard deviation, mean squared error, mean absolute error and mean average error considering 90% of the data, were calculated based on the quantity $\Delta P_{3D} - \Delta P_{simpl}$, where ΔP_{simpl} represent predictions based on the ROM or NN approaches. Similarly R^2 was calculated based on ΔP_{simpl} vs. P_{3D}. See Table 6 in the Appendix for corresponding numerical values. (For interpretation of the references to color in this figure legend, the reader is referred to the web version of this article.)

Table 2
Overview of data for stenotic segments for the test set and for training set sizes 1, 2 and 3.

Training set 1							
Number of segments: 529				Number of P–Q pairs: 5290			
	Avg	Std	10%	25%	50%	75%	90%
r_p [cm]	0.13	0.05	0.08	0.09	0.12	0.15	0.19
r_s [cm]	0.10	0.04	0.05	0.07	0.09	0.12	0.16
r_d [cm]	0.12	0.05	0.07	0.09	0.12	0.15	0.19
l [cm]	0.43	0.24	0.18	0.28	0.38	0.53	0.74
Q [ml/s]	1.21	1.32	0.14	0.31	0.77	1.53	2.95
ΔP_{3D} [mmHg]	1.43	4.35	0.03	0.10	0.33	1.07	3.21
Training set 2							
Number of segments: 936				Number of P–Q pairs: 8546			
	Avg	Std	10%	25%	50%	75%	90%
r_p [cm]	0.12	0.04	0.07	0.09	0.11	0.15	0.18
r_s [cm]	0.09	0.04	0.05	0.07	0.09	0.11	0.15
r_d [cm]	0.12	0.04	0.07	0.09	0.11	0.14	0.18
l [cm]	0.43	0.23	0.19	0.29	0.39	0.53	0.73
Q [ml/s]	1.19	1.28	0.14	0.31	0.77	1.54	2.89
ΔP_{3D} [mmHg]	1.53	4.00	0.03	0.12	0.42	1.36	3.64
Training set 3							
Number of segments: 1765				Number of P–Q pairs: 12 971			
	Avg	Std	10%	25%	50%	75%	90%
r_p [cm]	0.12	0.04	0.07	0.09	0.11	0.15	0.18
r_s [cm]	0.09	0.04	0.05	0.07	0.09	0.11	0.15
r_d [cm]	0.12	0.05	0.07	0.08	0.11	0.14	0.18
l [cm]	0.42	0.23	0.19	0.28	0.38	0.53	0.71
Q [ml/s]	1.09	1.23	0.11	0.28	0.68	1.42	2.67
ΔP_{3D} [mmHg]	1.34	3.58	0.03	0.10	0.35	1.14	3.22
Test set							
Number of segments: 381				Number of P–Q pairs: 3784			
	Avg	Std	10%	25%	50%	75%	90%
r_p [cm]	0.13	0.05	0.08	0.10	0.12	0.16	0.19
r_s [cm]	0.10	0.04	0.06	0.07	0.09	0.13	0.16
r_d [cm]	0.13	0.05	0.08	0.09	0.12	0.15	0.19
l [cm]	0.41	0.21	0.18	0.28	0.39	0.51	0.69
Q [ml/s]	1.33	1.42	0.18	0.38	0.84	1.75	3.25
ΔP_{3D} [mmHg]	1.37	4.32	0.03	0.09	0.31	1.10	2.87

3.2. Performance of simplified approaches for prediction of pressure loss

The error metrics for prediction of pressure loss across stenotic segments are shown in Fig. 4, and those for healthy segments are shown in Fig. 5. Each line represents the mean value of error metrics for a given approach (the error bars denote the standard deviation of the metrics across the ten random training splits). The color of the lines denotes the input feature set (X_1 blue, X_2 yellow and X_3 green) and each *column* corresponds to a particular NN modeling approach: from left $\Delta P_{\mathrm{NN},\Delta P}(X)$, $\Delta P_{\mathrm{NN},\epsilon_{\Delta P}}(X)$, $\Delta P_{\mathrm{NN},\Delta P}\left(X^{0\mathrm{D}}\right)$, $\Delta P_{\mathrm{NN},\epsilon_{\Delta P}}\left(X^{0\mathrm{D}}\right)$. Here we would like to remind the reader that $\Delta P_{\mathrm{NN},\Delta P}(X)$ refers to the purely data-driven NN model, and the remaining NN models have incorporated prior physics-based knowledge from the ROM — either through predicting the discrepancy $\epsilon\Delta P$ of the ROM and 3D iNS pressure loss, or through addition of the ROM pressure loss across the healthy (ΔP_h) or stenotic (ΔP_s) segment as indicated by $X^{0\mathrm{D}}$. The position on the x-axis corresponds with the dataset size (training set 1 $\rightarrow$ training set 3). In addition we evaluated the performance of the ROM on the same test set, and the resulting error metrics are shown for comparison (horizontal black line in each panel). The Appendix provides

Table 3
Overview of data for healthy segments for the test set and for training set sizes 1, 2 and 3.

Training set 1							
Number of segments: 804				Number of P–Q pairs: 8040			
	Avg	Std	10%	25%	50%	75%	90%
r_p [cm]	0.13	0.05	0.08	0.10	0.13	0.17	0.20
r_s [cm]	0.12	0.05	0.07	0.08	0.11	0.15	0.19
r_d [cm]	0.13	0.06	0.07	0.09	0.12	0.17	0.20
l [cm]	1.01	0.98	0.18	0.35	0.70	1.35	2.27
Q [ml/s]	1.30	1.50	0.14	0.31	0.79	1.66	3.26
ΔP_{3D} [mmHg]	0.67	1.59	0.00	0.04	0.17	0.61	1.74
Training set 2							
Number of segments: 1505				Number of P–Q pairs: 13 648			
	Avg	Std	10%	25%	50%	75%	90%
r_p [cm]	0.13	0.05	0.07	0.09	0.12	0.16	0.20
r_s [cm]	0.12	0.05	0.06	0.08	0.10	0.15	0.18
r_d [cm]	0.12	0.05	0.07	0.08	0.11	0.16	0.20
l [cm]	1.05	1.08	0.18	0.35	0.69	1.37	2.33
Q [ml/s]	1.30	1.49	0.13	0.31	0.79	1.67	3.22
ΔP_{3D} [mmHg]	0.83	1.96	0.00	0.05	0.21	0.76	2.18
Training set 3							
Number of segments: 2762				Number of P–Q pairs: 20 457			
	Avg	Std	10%	25%	50%	75%	90%
r_p [cm]	0.13	0.05	0.07	0.09	0.12	0.16	0.20
r_s [cm]	0.11	0.05	0.06	0.08	0.10	0.14	0.18
r_d [cm]	0.12	0.05	0.07	0.08	0.11	0.16	0.20
l [cm]	1.07	1.10	0.19	0.36	0.70	1.38	2.37
Q [ml/s]	1.21	1.42	0.12	0.29	0.72	1.54	3.04
ΔP_{3D} [mmHg]	0.79	1.86	0.00	0.05	0.20	0.72	2.04
Test set							
Number of segments: 574				Number of P–Q pairs: 5702			
	Avg	Std	10%	25%	50%	75%	90%
r_p [cm]	0.14	0.05	0.08	0.10	0.13	0.17	0.20
r_s [cm]	0.12	0.05	0.07	0.09	0.11	0.15	0.18
r_d [cm]	0.13	0.05	0.08	0.09	0.12	0.16	0.20
l [cm]	1.18	1.19	0.20	0.39	0.77	1.66	2.58
Q [ml/s]	1.42	1.54	0.17	0.38	0.88	1.87	3.56
ΔP_{3D} [mmHg]	0.95	2.75	0.00	0.06	0.21	0.75	2.17

tabulated versions of Fig. 4 (Table 5) and Fig. 5 (Table 6), where the numerical value of the error metrics for the NN approaches is given.

3.3. Performance of simplified approaches for prediction of FFR

We incorporated the simplified approaches for prediction of pressure losses across segments in a coronary network model to yield predictions of FFR, as illustrated in Fig. 1 and described in Section 2.6. Error metrics for evaluation of model performance for $\mathrm{FFR}_{\mathrm{simpl}}$ relative to $\mathrm{FFR}_{\mathrm{3D}}$ are presented in Fig. 6. Each line represents the mean value of error metrics for a given approach (the error bars denote the standard deviation of the metric across the ten random training splits). The color of the lines denotes the input feature set (X_1 blue, X_2 yellow and X_3 green) and each *column* corresponds to a particular NN modeling approach: from left $\mathrm{FFR}_{\mathrm{NN},\Delta P}(X)$, $\mathrm{FFR}_{\mathrm{NN},\epsilon_{\Delta P}}(X)$, $\mathrm{FFR}_{\mathrm{NN},\Delta P}\left(X^{\mathrm{0D}}\right)$, $\mathrm{FFR}_{\mathrm{NN},\epsilon_{\Delta P}}\left(X^{\mathrm{0D}}\right)$. $\mathrm{FFR}_{\mathrm{NN},\Delta P}(X)$ thus represents the FFR predictions when the purely data-driven NN models for predictions of pressure loss across stenotic and healthy segments were incorporated into the network

Table 4
Error metrics of $\mathrm{FFR}_{\mathrm{NN},\epsilon_{\Delta P}}\left(X_3^{\mathrm{0D}}\right)$ (trained on training set 3) vs. 3D iNS FFR predictions, on a per vessel basis. Here, N refers to the number of FFR locations (times three flow conditions = total number of FFR evaluations). Further, the bias, Std error and mean absolute error were calculated based on the quantity $\mathrm{FFR}_{\mathrm{3D}} - \mathrm{FFR}_{\mathrm{NN}}$. The minimum, maximum, 25th, 50th and 75th percentiles of $\mathrm{FFR}_{\mathrm{3D}}$ are also given. Abbreviations: LAD: left anterior descending, LCX: left circumflex artery, RCA: right coronary artery.

	N	Bias	Std error	MAE	min	max	25%	50%	75%
ALL	50 (150)	−0.005	0.021	0.016	0.34	0.99	0.82	0.90	0.94
LAD	26 (78)	−0.007	0.018	0.014	0.55	0.99	0.85	0.91	0.94
LCX	13 (39)	−0.006	0.025	0.022	0.34	0.98	0.64	0.87	0.95
RCA	11 (33)	0.003	0.019	0.016	0.56	0.95	0.83	0.87	0.90

solver. Further, the notation X^{0D} indicates that the ROM prediction of pressure loss (ΔP_h or ΔP_s) was included as input feature in the NNs for prediction of pressure loss across healthy and stenotic segments respectively. The position on the x-axis corresponds with the dataset size (training set 1 → training set 3). In addition we evaluated the performance of the ROM ($\mathrm{FFR}_{\mathrm{0D}}$) on the same test set and the resulting error metrics are shown for comparison (horizontal black line in each panel). The Appendix provides a tabulated version of Fig. 6 (Table 7) where the numerical values of the error metrics for the NN approaches are given.

Fig. 8 shows scatter and Bland–Altman plots of $\mathrm{FFR}_{\mathrm{0D}}$ and $\mathrm{FFR}_{\mathrm{NN}}$ vs. $\mathrm{FFR}_{\mathrm{3D}}$. $\mathrm{FFR}_{\mathrm{NN}}$ was obtained by averaging the individual predictions from the ten FFR predictions corresponding to $\mathrm{FFR}_{\mathrm{NN},\epsilon_{\Delta P}}\left(X_3^{\mathrm{0D}}\right)$ for training set size 3. In the scatter plots, the horizontal and vertical dashed lines represent the FFR cut-off value for classifying ischemia causing stenoses ($\mathrm{FFR} \leq 0.8$). In the Bland–Altman plots, horizontal lines represent ± 2 standard deviations of model error (black) and of repeated FFR measurements (red). The mean difference ± standard errors for the ROM and NN augmented ROM with respect to $\mathrm{FFR}_{\mathrm{3D}}$ were -0.042 ± 0.034 and −0.005 ±0.021 respectively. Standard deviation of repeated FFR measurement is 0.018 [45]. Further, Table 4 provides a break up of the bias, std error and mean absolute error of $\mathrm{FFR}_{\mathrm{NN}}$ vs. $\mathrm{FFR}_{\mathrm{3D}}$ on a per vessel basis (LAD: left anterior descending, LCX: left circumflex artery, RCA: right coronary artery). The minimum, maximum, 25th, 50th and 75th percentiles of $\mathrm{FFR}_{\mathrm{3D}}$ are also presented.

Finally, Fig. 7 presents error metrics of the simplified approaches for prediction of FFR with respect to invasively measured FFR. In addition, corresponding error metrics for $\mathrm{FFR}_{\mathrm{3D}}$ are also indicated (horizontal dotted lines). The Appendix provides a tabulated version of Fig. 7 (Table 8) where the numerical values of the error metrics for the NN approaches are given.

4. Discussion

We analyzed the effect of incorporating prior physics-based knowledge in the learning process for prediction of pressure and FFR in coronary arteries. Fully connected feed forward NNs were trained to predict pressure losses obtained by solution of the 3D iNS equations in segmented coronary arteries. We incorporated prior physics-based knowledge from a reduced-order model of blood flow in stenotic and healthy coronary arteries. The prior information was included by training NNs to (1) predict the discrepancy between the reduced-order model and 3D iNS pressure loss rather than pressure directly and (2) incorporated in the learning process by including the ROM pressure loss prediction as a feature. The physics informed NNs were compared with a corresponding purely data-driven NN for three different training sets with increasing amount of data. Both approaches for incorporation of prior knowledge from the ROM significantly improved prediction of pressure losses across healthy and stenotic segments relative to the purely data-driven approach, especially for lower amounts of training data.

4.1. Prediction of pressure loss

We separated the coronary domain into healthy and stenotic segments. For each segment, solutions of 3D iNS for several different pressure and flow states served as the basis for the dataset for training NNs to predict the pressure losses across the segments.

Four methods for predicting ΔP_{3D} with NNs were applied. First, a naive *pure machine learning* approach trained a NN to predict ΔP_{3D} without incorporation of any prior physical knowledge, while the remaining approaches

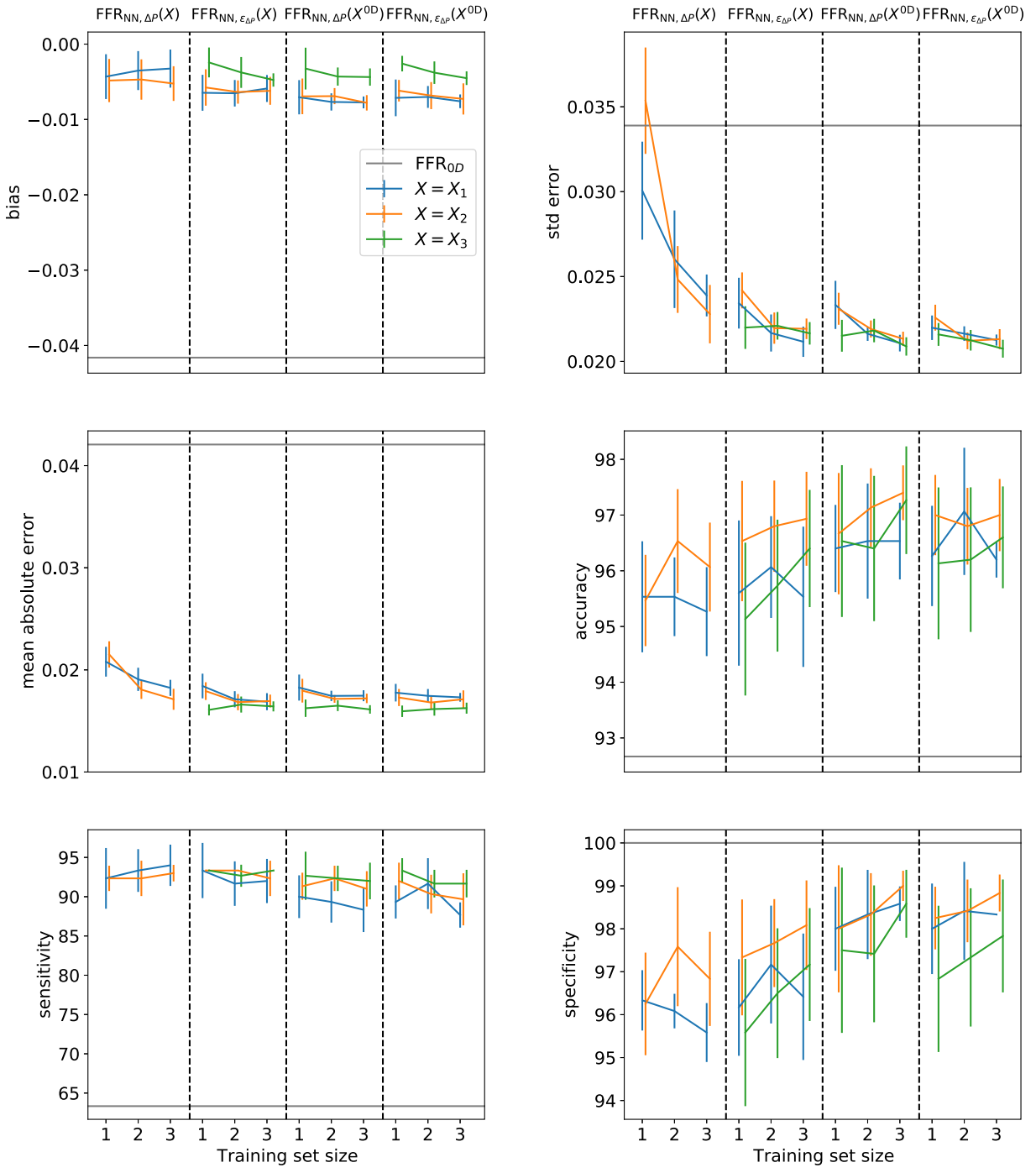

Fig. 6. Results for machine learning approaches for prediction of FFR vs. FFR_{3D}. The values presented by each line are the average of the metric across the 10 random training splits, while the vertical lines represent the standard deviation of the metric across the training splits. The bias, error standard deviation and mean absolute errors were calculated based on the quantity $FFR_{3D} - FFR_{simpl}$, where FFR_{simpl} represent predictions based on the ROM or NN approaches. The accuracy, sensitivity and specificity were calculated based on dichotomized data ($FFR_{3D} < 0.8$). All metrics are without units. See Table 7 in the Appendix for corresponding numerical values.

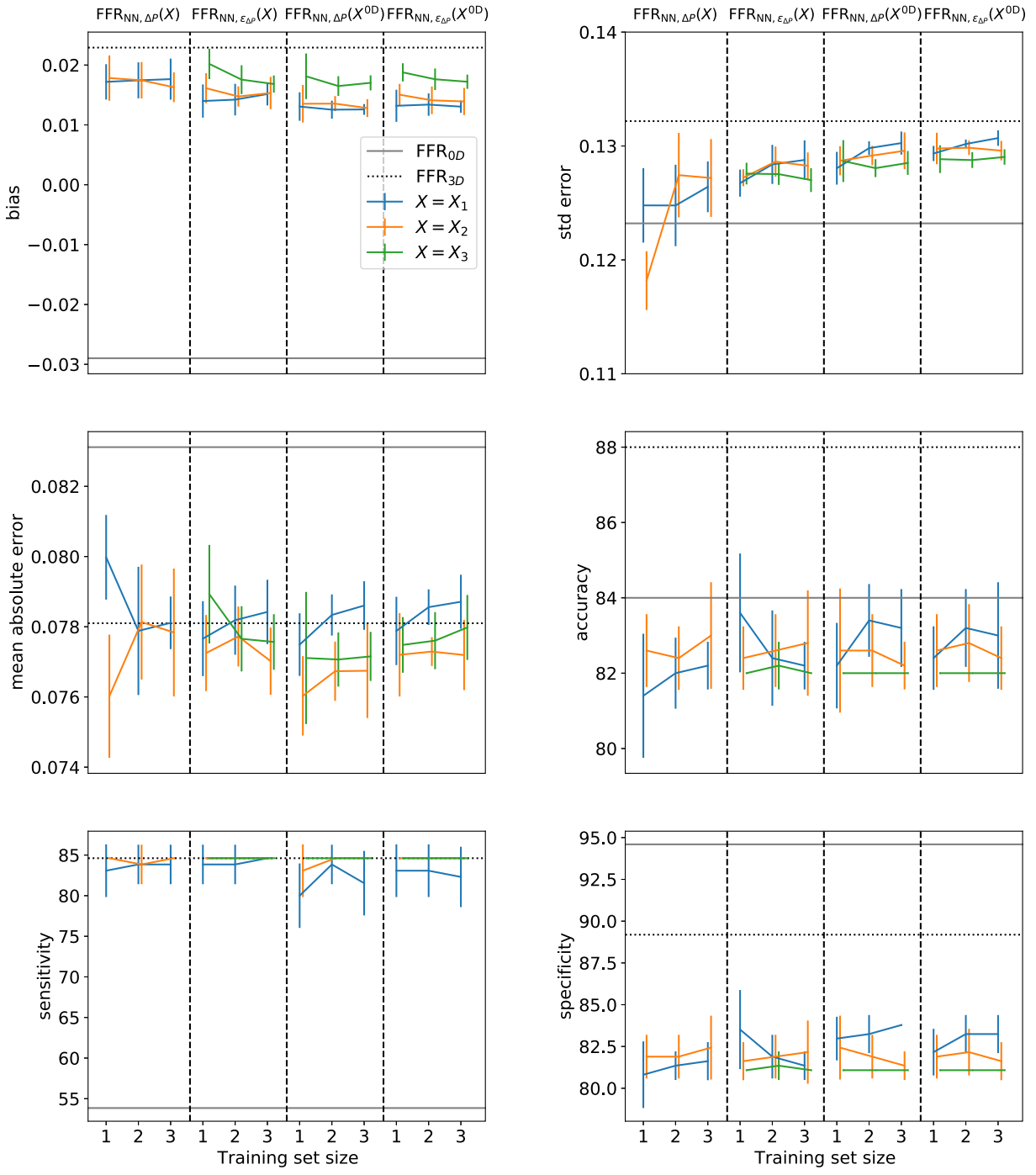

Fig. 7. Results for machine learning approaches for prediction of FFR vs. FFR_{meas}. The values presented by each line are the average of the metric across the 10 random training splits, while the vertical lines represent the standard deviation of the metric across the training splits. The bias, error standard deviation and mean absolute errors were calculated based on the quantity $\text{FFR}_{\text{meas}} - \text{FFR}_{\text{pred}}$, where FFR_{pred} represent predictions based on the 3D model, ROM or NN approaches. The accuracy, sensitivity and specificity were calculated based on dichotomized data ($\text{FFR}_{\text{meas}} < 0.8$). All metrics are without units. See Table 8 in the Appendix for corresponding numerical values.

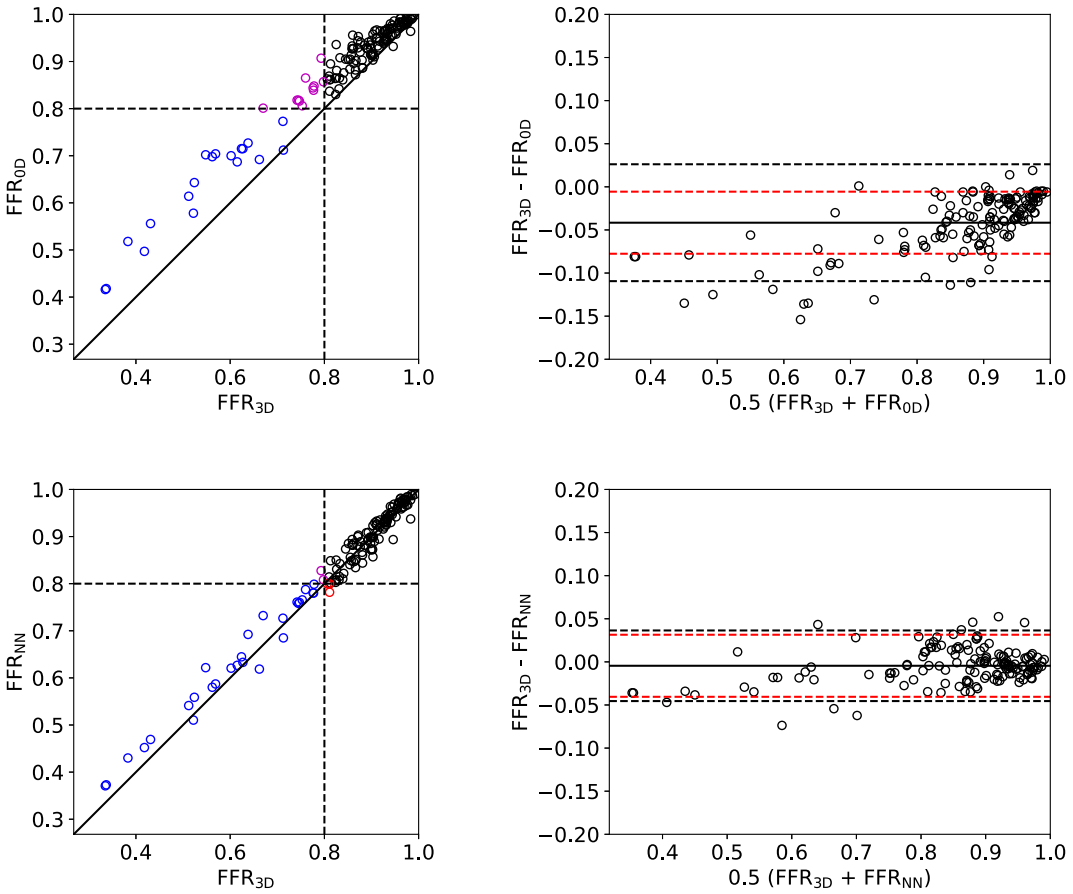

Fig. 8. Scatter and Bland–Altman plots of ROM predictions (top) and NN augmented ROM predictions (bottom) of FFR relative to 3D iNS FFR predictions. $\mathrm{FFR}_{\mathrm{NN}}$ was calculated based on the mean prediction (corresponding the 10 random training/validation splits) for those obtained by the combined physics informed approach, $\mathrm{FFR}_{\mathrm{NN},\epsilon_{\Delta P}}\left(X_3^{\mathrm{0D}}\right)$ when trained on dataset size 3. In scatter plots, the horizontal and vertical dashed lines represent the FFR cut-off value for classifying ischemia causing stenoses. In the Bland–Altman plots, horizontal lines represent ± 2 standard deviations of model error (black) and of repeated FFR measurements (red). The mean difference ± standard errors for the ROM and NN augmented ROM with respect to $\mathrm{FFR}_{\mathrm{3D}}$ were -0.0416 ± 0.034 and −0.0045 ±0.020 respectively.

included prior knowledge either through prediction of the discrepancy function ($\Delta P_{\mathrm{3D}} - \Delta P_{\mathrm{0D}}$), by including ΔP_{0D} as an input-feature, or through a combination of the two former approaches.

The top left panel of Fig. 4 shows that all NN-approaches achieved similar values in terms of the bias in prediction of pressure loss across stenotic segments (mean values ranging between 0.01–0.07 mmHg), all of which represent major reductions relative to the bias of the pure physics-based approach (0.56). For the remaining error metrics (MAE, std error, MSE, R^2), which better capture the NNs ability to predict pressure losses for individual segments, the effect of including physics-based information in the design or learning process, substantially impacted the results and dependence on data.

4.1.1. Effect of training-set size

A key obstacle for successful application of NNs is the amount of suitable data available for the task at hand. When too little data is available, NNs may generalize poorly and provide erroneous predictions in regions that are poorly represented in the dataset, and for unseen parameter combinations.

From Fig. 4, considering input feature X_1, we can observe that the error metrics for all approaches had a tendency to improve with the inclusion of more data. The most notable improvement was observed for the pure data-driven learning approach (MAE: 0.39 to 0.33 (15% reduction), MSE: 2.4 to 1.47 (39%), std: 1.54 to 1.21 (21%), R^2: 0.87 to 0.92 (6% improvement) from training set sizes 1 to 3). The incorporation of physics-based information reduced

such dependence. For these approaches the MAE and MSE for training sets 1 and 3 (with percent change between these training set reported in parentheses) follow. For $\Delta P_{\mathrm{NN},\epsilon_{\Delta P}}(X_1)$ MAE went from 0.33 to 0.30 (9%) and MSE from 1.38 to 1.09 (21%). For $\Delta P_{\mathrm{NN},\Delta P}\left(X_1^{\mathrm{0D}}\right)$ MAE went from 0.33 to 0.30 (9%) and MSE from 1.29 to 0.99 (23%). For $\Delta P_{\mathrm{NN},\epsilon_{\Delta P}}\left(X_1^{\mathrm{0D}}\right)$ MAE went from 0.32 to 0.30 (6%) and MSE from 1.10 to 1.00 (9%).

This reveals that including physics-based knowledge reduced the amount of data required to train NNs to a certain level of accuracy. Interestingly, the middle right plot in Fig. 4 shows that, when excluding the highest 10% percent of pressure losses, differences in mean absolute error between purely data-driven and physics informed NNs were much lower. This indicates that the physics-informed approaches performed better on regions poorly represented in the dataset. Moreover, we note that both pure data-driven NNs and physics-informed NNs performed similarly on the training datasets (see supplementary Fig. A.2) despite the fact that physics-informed NNs performed much better on the test dataset. This suggests that the purely data-driven NNs may be more prone to overfit to the training data in comparison to physics-informed NNs.

By both reducing the need for data and improving the generalization of NNs, physics informed machine learning might in many circumstances offer the best of both worlds, and these results motivate similar approaches for problems with sparse data in particular.

4.1.2. Different approaches for incorporation of prior physics-based knowledge

A variety of approaches for incorporation of prior knowledge into machine learning have been proposed [7,11]. In this study, we proposed three such approaches for NN based prediction of pressure losses in coronary arteries. First, we proposed training NNs to predict model discrepancy of the ROM. Second, we included the ROM prediction of pressure loss as a feature. Finally, we trained NNs to predict the discrepancy while also using the ROM prediction as an input.

Still considering results for pressure drop across stenotic segments, *columns* 2–4 in Fig. 4 provide error metrics for the different approaches for incorporation of physics-based information in the learning process. The mean squared errors were 1.38 (0.13), 1.29 (0.26) and 1.10 (0.06) considering training set size 1, for $\Delta P_{\mathrm{NN},\epsilon_{\Delta P}}(X_1)$, $\Delta P_{\mathrm{NN},\Delta P}\left(X_1^{\mathrm{0D}}\right)$, $\Delta P_{\mathrm{NN},\epsilon_{\Delta P}}\left(X_1^{\mathrm{0D}}\right)$ respectively (the values in the parentheses represent the standard deviation of the error for the ten random learning/validation splits). Corresponding values for training set size 3 were 1.09 (0.13), 0.99 (0.05) and 1.00 (0.04). Similar trends may be seen for the std. error and R^2 score. The approach which included physics-based information as a feature, $\Delta P_{\mathrm{NN},\Delta P}$ thus achieved better results than the discrepancy method, $\Delta P_{\mathrm{NN},\epsilon_{\Delta P}}$. A possible explanation for this might be that the former approach allows for more interaction between ROM predictions and other features. If the physics-based prediction is accurate the NN can easily learn to predict the true quantity and if biases are present, then correlations with these and the other features may be learned. The inclusion of physics-based simulations as features is perhaps the most common approach for including prior physics-based information in machine learning [9–12]. Our results indicate that a combined approach, $\Delta P_{\mathrm{NN},\epsilon_{\Delta P}}\left(X^{\mathrm{0D}}\right)$ is less sensitive to dataset size and split and provides the most reliable results for lower dataset sizes.

The physics informed approaches considered in this study do not require an explicit trade off between physics-based knowledge and data, which is in contrast to another approach that informs the NNs by incorporating a physics-based term to the loss function [13,46,47]. The latter approach for including prior physics-based information may enable machine learning with very little data, since part of the training only relates to evaluation of the physical loss term which can be performed without "real" data. However in the limit when no additional real data is included, one cannot expect better predictions than from the underlying physical model. In practice a choice about the balance between data and governing physics must be made when specifying the algorithm. In contrast, the inclusion of the physics-based model prediction allows the machine learning algorithm to learn this balance by itself, and thus exploiting the power of the data-driven learning algorithm. On the other hand, our approaches do not explicitly penalize violation of the governing physics, a property that might be beneficial in some applications [11].

4.1.3. Effect of incorporation of 3D geometrical data and upstream dynamics

Most physics-based reduced-order models for prediction of pressure drop in arteries and across stenoses assume axisymmetry and do not incorporate upstream dynamics [21,38,48]. However, the pressure drop along a segment is not entirely a local phenomena, and in addition to the flow (which depends on upstream and downstream dynamics) geometrical asymmetries and eccentricity may effect the pressure drop along a segment [38,49,50]. We thus sought to explicitly evaluate the impact of these assumptions by comparing feature-arrays which represented only

local dynamics and idealized geometric axisymmetric properties with arrays that contain more generic geometric information and upstream dynamics. In feature-array X_1 we included the inputs most commonly observed in reduced-order models for prediction of pressure loss across stenoses. To incorporate more geometrical information, input feature-array X_2 included the most important components of a principal components analysis of the radius and eccentricity along the centerline, as well as the minimum cross sectional radius in the segment. Feature-array X_3 augmented X_2 with flow-separation related pressure losses and changes to the dynamic pressure in a region 1 cm upstream of the beginning of the segment.

The addition of more geometrical data incrementally improved predictions across stenotic segments for the physics informed NNs, as illustrated by the improvements in error metrics from going from X_1 (blue lines) to X_2 (orange lines) in Fig. 4 (*e.g.* MAE: 0.30 to 0.29 for all physics-informed approaches considering training set size 3). Such trends were less prominent for healthy segments (see Fig. 5), where no reliable improvement was seen by adding more geometrical data to the physics informed approaches (MAE: 0.25 to 0.25 for both $\Delta P_{\mathrm{NN},\epsilon_{\Delta P}}(X)$ and $\Delta P_{\mathrm{NN},\Delta P}\left(X^{\mathrm{0D}}\right)$ and MAE :0.26 to 0.25 for $\Delta P_{\mathrm{NN},\epsilon_{\Delta P}}\left(X^{\mathrm{0D}}\right)$). This may be a result of the fact that stenotic and healthy segments were differentiated based on the relative smoothness of local variation in radius. As, such healthy segments tend to be relatively straight and much of the geometrical variation is already filtered out.

In contrast to geometric information, the addition of upstream pressure data influenced the prediction capacity across both stenotic and healthy segments, but with a more notable improvement across healthy segments, illustrated by the improvements in error metrics from X_2 (orange lines) to X_3 (green lines) in Figs. 4 and 5. For instance, the mean squared error was reduced from 0.46 to 0.35 (24% reduction) for healthy segments (considering the combined physics informed approach for data-set size 3), while corresponding values for stenotic segments were 0.96 to 0.89 (7%). Streamline disturbances and flow separation may occur distal of stenoses and will effect the pressure drop at such regions [38], which may explain why prediction performance of healthy segments was particularly improved by the inclusion of upstream information.

Similarities and differences in pressure loss across stenotic and healthy segments. The previous two paragraphs highlight different effects on prediction of pressure across stenotic and healthy segments for different input features. In Section 4.1.1 we stated a clear dependence on dataset size for error metrics for prediction of pressure loss across stenotic segments for the purely data-driven approach. Incorporation of physics-based information to the NN's reduced such dependence. See input feature X_1 (blue lines) in Fig. 4. While a clear dependence is seen for the purely data-driven approach also in the case of prediction of pressure loss across healthy segments (first column in Fig. 5), it is not as evident for the physics informed approaches (*columns* 2–4). Hence the learning seems to be close to saturation already for the lowest data-set size when including physics-based information for the healthy segments.

For some error metrics (std. error, and MSE) we observed examples of non-monotone relation between error metrics and data-set size, and even worsening of metrics with increasing data-set size (*columns* three and four in the MSE and std. plots in Fig. 5). For prediction of pressure loss across stenotic segments occurrence of non-monotone relation between error metrics and data-set size was seen for the expanded input features X_2 and X_3 (*columns* three and four in the MSE and std plots in Fig. 4). In terms of the mean absolute error however, all approaches (both for stenotic and healthy segments and for all feature-sets) demonstrated a monotone improvement for increased data-set size. This should be seen in relation with the origin of the added training data going from training data size $1 \rightarrow 3$. For instance, going from training set size 2 to training set size 3, consisted in adding data from coronary trees without FFR measurements (*i.e.* without suspected CAD) and coronary trees from a prospective population with low prevalence of severe CAD. This partly explains the fact that most predictions were improved (indicated by the improvement in MAE), while at the same time showing non-monotone relation in terms of predictions with higher absolute errors (indicated by the behavior of MSE and std error).

4.2. Prediction of FFR

Several approaches for non-invasive FFR prediction based on reduced-order physics-based models have been developed [19–22]. Moreover, Itu. et al. [27] trained a neural network to reproduce FFR predictions based on a reduced-order model akin to the ROM in this work. The model denoted $\mathrm{CT}-\mathrm{FFR}_{\mathrm{ML}}$ was trained on 12,000 synthetically generated coronary artery models, where ground truth predictions based on a physics-based reduced-order model were used as reference. This approach is thus still limited by the shortcomings and assumptions related

to the reduced-order model as opposed to 3D iNS. Further, Sankaran et al. trained a bootstrapped aggregated decision tree, which included geometrical, clinical and reduced-order model input-features [9,10]. The machine learning regressor was trained to predict full $\mathrm{FFR}_{\mathrm{CT}}$ at selected centerline points, with the primary motive to calculate sensitivity indices in uncertainty quantification analysis.

In contrast to previous works, we have explicitly focused on training NNs to predict pressure losses in both healthy and diseased coronary artery segments. We incorporated the trained NNs into a coronary network model to predict FFR. The discrepancy between the combined physics-informed NN FFR predictions and 3D FFR had a standard deviation of 0.022 for the lowest dataset size (see *column* four, feature-set X_1 in Fig. 6). In comparison, the purely data-driven NN had a standard deviation of 0.03 for the smallest data-set size (see column one, feature-set X_1 in Fig. 6). Dependence on data-set size was seen for the purely data-driven NN, where standard deviation was reduced to 0.024 (20% reduction) in training-set size 3 (the corresponding value for the combined physics-based approach was 0.021). In comparison the standard deviation of repeated FFR measurements is 0.018 according to a previous study [45]. Furthermore Fig. 8 illustrates the reduction in both bias and scatter resulting from the NN-augmented FFR models (exemplified by $\mathrm{FFR}_{\mathrm{NN},\epsilon_{\Delta P}}\left(X_3^{\mathrm{0D}}\right)$), relative to the purely physics based FFR model.

The incorporation of more geometrical data regarding segment shape and eccentricity and inclusion of upstream pressure dynamics resulted in incremental reduction in mean absolute error of NN based FFR versus 3D iNS FFR (see mean absolute error plot in Fig. 6). Still, even with the inclusion of these features, the reduced-order model can be considered a very coarse representation of the 3D problem. To improve predictions, incorporation of more of the geometrical information is likely necessary. This could be obtained by extended application of principal component analysis or by application of auto-encoders of the 3D mesh/domain [51]. However, in order to successfully train NNs to incorporate such subtle information might require significantly more data than even the largest dataset in this study.

It is known that the LAD is the most affected vessel by CAD, and also that most of FFR assessments are for the LAD. Moreover, previous studies have shown that the accuracy of FFR prediction can vary according to the vessel [29]. We assessed the potential influence of such bias by evaluating the performance of the NN augmented ROMs (exemplified by $\mathrm{FFR}_{\mathrm{NN},\epsilon_{\Delta P}}\left(X_3^{\mathrm{0D}}\right)$ and corresponding to Fig. 8) on a per vessel basis. Table 4 shows that the MAE and std. error of $\mathrm{FFR}_{\mathrm{NN}}$ vs. $\mathrm{FFR}_{\mathrm{3D}}$ were similar in the LAD and RCA, despite the fact that almost 52% of locations were in the LAD while only 22% were in the RCA. The std error and MAE were substantially higher in the LCX (26% of cases). However, as can be seen from the distribution of $\mathrm{FFR}_{\mathrm{3D}}$, there were more severe (low) FFR cases in the LCX. This indicates that the differences in performance to predict FFR by the NN augmented FFR model were more related to the severity of CAD (*i.e.* more extreme geometries and pressure drops), rather than related to an implicit bias concerning the frequency of CAD in a vessel.

In Fig. 7 the different models for prediction of FFR are compared with invasive measurements. As can be seen from the top left plot, the purely physics-based ROM, and NN-augmented ROMs were biased in opposite directions. This may be seen in relation with the lower sensitivity, but higher specificity for the purely physics-based ROM. The most comprehensive model considered in this work, namely the full 3D iNS model produced the best trade-off between sensitivity and specificity, indicating that model differences had an effect on classification of ischemia. However, the 3D iNS model also resulted in the highest standard deviation between measurements and predictions. Hence there is not necessarily a direct link between model complexity and standard deviation of errors between model prediction and invasive FFR. With model errors close to the standard deviation of repeated FFR measurements, intrinsic uncertainties related to geometry, and the setting of boundary-conditions (*i.e.* flow-distribution, and the effects of adenosine) dominate [29]. Thus even though the potential exists for further improvement of the NN augmented reduced-order model (relative to the full 3D iNS model), such improvements are unlikely to improve prediction errors relative to invasive measurements substantially.

Currently, models based on *very* different assumptions about the underlying physics perform to similar levels of accuracy with respect to invasive FFR measurements [52]. In some cases, the accuracy in FFR prediction may come at the cost of physically implausible predictions for other variables such as the volumetric flow rate [52]. This may be an important issue to consider during model design, particularly if FFR is not the only model quantity of interest. Thus, even though further improvements to the ROM relative to the 3D iNS model may not result in more accurate FFR prediction, they may be crucial for estimation of other clinical indices.

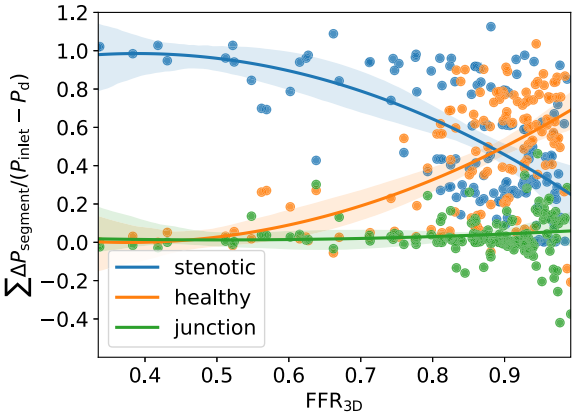

Fig. A.1. Cumulative pressure drop for segment types as a ratio of total pressure drop from the coronary inlet to the measurement location.

5. Limitations and future work

Several factors are necessary for successful application of neural networks. The perhaps most important aspect in this context relates to the amount of data available for training. We found that the incorporation of physics-based prior knowledge efficiently improved NN pressure loss predictions in cases with sparse data. There are, however, other factors that have an effect on the performance of NNs, and even though NNs are universal function approximators, the exact design and input features that will predict a relation optimally is not known a priori. In this context, we performed hyperparameter searches that resulted in the design of the neural networks used in this study. In addition we applied other common approaches, such as adopting validation/learning splits in attempts to avoid over-fitting. We also explored incorporation of other features, such as more geometrical information from radius and eccentricity information through including more PCA components, and information regarding curvature, however without providing improvement in results (not shown here). The latter is somewhat surprising given that previous studies indicate that inclusion of curvature to lumped parameter models could improve predictions relative to 3D CFD simulations [53,54]. One might question if the physical effect of curvature is correlated with some combination of other included input features (and thus partly learned, *e.g.* it is known that the effect of curvature depends on the Reynolds number, which was indirectly included) or alternatively if there were insufficient variability in our training data to learn the impact of curvature. Nevertheless, even though there is still the possibility that other means of providing relevant input features could lead to improved results, such alterations should have the same potential of improvement on all NN approaches.

The choice of including cumulative upstream information from 1 cm upstream of the segment was based on inspection of flow separation regions in relevant stenoses. However, the effective length of disturbed/separated flow is known to vary according to stenosis severity and Reynolds number [38]. Predictions by fully connected feed forward neural networks are restricted by the supplied input features. This complicates incorporation of information that is based on predictions of nearby segments, since such information has to be explicitly included as features. The inclusion of upstream information improved prediction of pressure by the NNs, however more sophisticated (recurrent) neural networks and particularly Long Short-Term Memory networks which are designed to allow information of nearby predictions (in time or space) to persist might be more suited to include such information and might lead to improved results [55,56].

The simplified coronary network model considered in this study separated the coronary domain into healthy, stenotic and junction regions. FFR predictions result from the nonlinear interaction of pressure losses across the segments and junctions (in relation with the prescribed boundary-conditions). We chose to focus on prediction of pressure loss across stenotic and healthy segments (and not pressure losses across junctions) based on an analysis where the relative importance of segment types was quantified (see supplementary Fig. A.1). This revealed that the relative importance of pressure losses at junctions was small in comparison to those seen across healthy and in particular stenotic segments, and that improvements in the junction model would not reduce standard deviation of FFR predicted by the ROM with respect to 3D iNS FFR. However for individual cases, errors introduced by the

junction model were not negligible and might effect the sensitivity and specificity for classifying the significance of the stenoses (FFR ≤ 0.8) and will thus be considered in future works.

6. Conclusion

Neural networks can in theory represent any functional relationship between inputs and output. However, in many applications the amount of data required to obtain this is prohibitive. We proposed that incorporating physics-based knowledge when designing and training NNs may reduce this burden and investigated this concept when training NNs for prediction of pressure drop in coronary arteries.

We evaluated three methods to incorporate physics-based knowledge in the learning process: learning the model discrepancy between ROM and 3D iNS, providing the physics-based ROM's predictions as an input feature, and the combination of both prior approaches. All three approaches significantly improved the prediction capacity of NN predictions of pressure loss relative to an uninformed approach. In addition, the inclusion of prior physics significantly reduced the amount of data required to obtain reliable and accurate predictions. The performance of the three approaches was similar, however subtle benefits were seen by the approach that included the ROM pressure loss as a feature, and the combined approach resulted in the most reliable prediction for the lowest dataset size considered.

Although the purely data-driven NN performed better than the physics-based reduced-order model relative to 3D iNS, this was not reliably obtained until enough data was used to train the NN. Further, the predictions by the informed NNs remained better than predictions by the purely data-driven NN for all data-sizes considered. As such, the combination of physics-based knowledge with data-driven machine learning leveraged the best of both worlds and motivates application of this combined approach for problems with sparse data.

The incorporation of informed NN predictions of coronary segment pressure losses in a coronary network model resulted in FFR predictions with standard deviation with respect to 3D iNS FFR of 0.021 for the lowest dataset size considered. This is comparable with the standard deviation of repeated FFR measurements, which is 0.018. Incorporation of features that represent more of the geometry and better representation of non-local effects might be needed to further reduce the error.

Finally, we note that the diagnostic accuracy of FFR predictions versus invasive FFR measurements varied for the different models, i.e. the full 3D iNS, the physics-based and the machine learning augmented ROMs. This indicates that the level of detail by which a physical process is modeled can have an impact on the diagnostic accuracy of the resulting FFR prediction algorithm. However, with uncertainty in predicted FFR being dominated by intrinsic uncertainties related to geometry and boundary-conditions, it is unlikely that further improvements in ROM predictions with respect to 3D iNS FFR will significantly and reliably improve predictions of invasive FFR measurements.

Declaration of competing interest

The authors declare that they have no known competing financial interests or personal relationships that could have appeared to influence the work reported in this paper.

Acknowledgments

We would like to thank NTNU Health (Strategic Research Area at the Norwegian University of Science and Technology) for funding this study. Furthermore the 3D iNS simulations were performed on resources provided by UNINETT Sigma2 — the National Infrastructure for High Performance Computing and Data Storage in Norway.

Appendix. Results

A.1. Tabulated results

See Tables 5–8 for tabulated error metrics corresponding to Figs. 4–7 .

Table 5
Results for machine learning approaches for prediction of pressure losses across stenotic segments. The values represent the averages (standard deviation) of the metrics across the 10 random training splits. The bias, standard deviation, mean squared error, mean absolute error and mean absolute error considering 90% of the data, were calculated based on the quantity $\Delta P_{3D} - \Delta P_{NN}$, where ΔP_{NN} represent predictions based on the NN approaches. Similarly R^2 was calculated based on ΔP_{NN} vs. P_{3D}.

Training-size	$\Delta P_{NN,\Delta P}(X)$		$\Delta P_{NN,\epsilon_{\Delta P}}(X)$			$\Delta P_{NN,\Delta P}\left(X^{0D}\right)$			$\Delta P_{NN,\epsilon_{\Delta P}}\left(X^{0D}\right)$		
	X_1	X_2	X_1	X_2	X_3	X_1	X_2	X_3	X_1	X_2	X_3
	Bias										
1	0.05 (0.05)	0.05 (0.02)	0.04 (0.02)	0.04 (0.02)	0.05 (0.02)	0.05 (0.03)	0.05 (0.03)	0.07 (0.03)	0.04 (0.02)	0.04 (0.03)	0.07 (0.02)
2	0.02 (0.04)	0.02 (0.04)	0.03 (0.03)	0.03 (0.03)	0.04 (0.02)	0.04 (0.02)	0.04 (0.02)	0.06 (0.03)	0.02 (0.02)	0.03 (0.02)	0.04 (0.02)
3	0.01 (0.02)	0.01 (0.03)	0.02 (0.02)	0.03 (0.02)	0.05 (0.01)	0.02 (0.01)	0.04 (0.02)	0.05 (0.02)	0.02 (0.01)	0.04 (0.03)	0.05 (0.01)
	Std error										
1	1.54 (0.17)	1.79 (0.14)	1.17 (0.06)	1.14 (0.06)	1.05 (0.08)	1.13 (0.11)	1.04 (0.05)	0.98 (0.08)	1.05 (0.03)	1.00 (0.06)	0.96 (0.05)
2	1.36 (0.17)	1.22 (0.14)	1.08 (0.08)	1.04 (0.05)	1.02 (0.05)	1.04 (0.02)	1.00 (0.04)	1.00 (0.04)	1.01 (0.02)	0.98 (0.03)	0.96 (0.04)
3	1.21 (0.09)	1.21 (0.12)	1.04 (0.06)	1.04 (0.06)	1.06 (0.05)	0.99 (0.02)	0.97 (0.04)	0.95 (0.03)	1.00 (0.02)	0.98 (0.04)	0.94 (0.02)
	Mean absolute error										
1	0.39 (0.02)	0.38 (0.01)	0.33 (0.01)	0.31 (0.01)	0.29 (0.01)	0.33 (0.01)	0.31 (0.01)	0.30 (0.01)	0.32 (0.00)	0.30 (0.01)	0.29 (0.01)
2	0.34 (0.01)	0.32 (0.01)	0.31 (0.01)	0.29 (0.01)	0.28 (0.01)	0.31 (0.01)	0.29 (0.01)	0.29 (0.01)	0.31 (0.00)	0.29 (0.01)	0.28 (0.01)
3	0.33 (0.01)	0.31 (0.01)	0.30 (0.01)	0.29 (0.01)	0.28 (0.01)	0.30 (0.00)	0.29 (0.00)	0.28 (0.01)	0.30 (0.00)	0.29 (0.01)	0.28 (0.00)
	Mean absolute error 90%										
1	0.18 (0.01)	0.17 (0.00)	0.17 (0.01)	0.16 (0.00)	0.16 (0.01)	0.17 (0.00)	0.16 (0.00)	0.15 (0.00)	0.17 (0.00)	0.16 (0.01)	0.15 (0.00)
2	0.17 (0.00)	0.17 (0.01)	0.17 (0.00)	0.16 (0.00)	0.15 (0.01)	0.16 (0.01)	0.15 (0.00)	0.15 (0.01)	0.16 (0.00)	0.15 (0.00)	0.15 (0.00)
3	0.17 (0.00)	0.16 (0.01)	0.16 (0.00)	0.15 (0.00)	0.15 (0.00)	0.16 (0.00)	0.15 (0.00)	0.14 (0.00)	0.16 (0.00)	0.15 (0.00)	0.14 (0.00)
	Mean squared error										
1	2.40 (0.52)	3.22 (0.50)	1.38 (0.13)	1.29 (0.13)	1.11 (0.17)	1.29 (0.26)	1.10 (0.11)	0.98 (0.17)	1.10 (0.06)	1.01 (0.12)	0.93 (0.09)
2	1.87 (0.46)	1.51 (0.36)	1.17 (0.17)	1.09 (0.10)	1.04 (0.09)	1.08 (0.05)	1.01 (0.07)	1.00 (0.07)	1.02 (0.05)	0.97 (0.06)	0.92 (0.08)
3	1.47 (0.21)	1.47 (0.28)	1.09 (0.13)	1.09 (0.12)	1.12 (0.11)	0.99 (0.05)	0.95 (0.08)	0.90 (0.07)	1.00 (0.04)	0.96 (0.07)	0.89 (0.04)
	R^2										
1	0.87 (0.03)	0.83 (0.03)	0.93 (0.01)	0.93 (0.01)	0.94 (0.01)	0.93 (0.01)	0.94 (0.01)	0.95 (0.01)	0.94 (0.00)	0.95 (0.01)	0.95 (0.00)
2	0.90 (0.02)	0.92 (0.02)	0.94 (0.01)	0.94 (0.01)	0.94 (0.01)	0.94 (0.00)	0.95 (0.00)	0.95 (0.00)	0.95 (0.00)	0.95 (0.00)	0.95 (0.00)
3	0.92 (0.01)	0.92 (0.02)	0.94 (0.01)	0.94 (0.01)	0.94 (0.01)	0.95 (0.00)	0.95 (0.00)	0.95 (0.00)	0.95 (0.00)	0.95 (0.00)	0.95 (0.00)

Table 6
Results for machine learning approaches for prediction of pressure losses across healthy segments. The values represent the averages (standard deviation) of the metrics across the 10 random training splits. The bias, standard deviation, mean squared error, mean absolute error and mean absolute error considering 90% of the data, were calculated based on the quantity $\Delta P_{3D} - \Delta P_{NN}$, where ΔP_{NN} represent predictions based on the NN approaches. Similarly R^2 was calculated based on ΔP_{NN} vs. P_{3D}.

Training-size	$\Delta P_{NN,\Delta P}(X)$		$\Delta P_{NN,\epsilon_{\Delta P}}(X)$			$\Delta P_{NN,\Delta P}\left(X^{0D}\right)$			$\Delta P_{NN,\epsilon_{\Delta P}}\left(X^{0D}\right)$		
	X_1	X_2	X_1	X_2	X_3	X_1	X_2	X_3	X_1	X_2	X_3
	Bias										
1	−0.02 (0.04)	−0.02 (0.03)	−0.02 (0.02)	−0.02 (0.02)	0.00 (0.02)	−0.01 (0.03)	−0.02 (0.02)	−0.01 (0.03)	−0.02 (0.03)	−0.02 (0.03)	−0.02 (0.02)
2	−0.07 (0.03)	−0.01 (0.02)	−0.03 (0.02)	−0.01 (0.01)	−0.00 (0.01)	−0.01 (0.01)	−0.02 (0.01)	0.01 (0.02)	−0.02 (0.01)	−0.01 (0.02)	0.00 (0.02)
3	−0.04 (0.02)	−0.01 (0.02)	−0.03 (0.01)	−0.01 (0.01)	0.01 (0.01)	−0.01 (0.01)	−0.00 (0.01)	0.01 (0.01)	−0.01 (0.01)	−0.01 (0.02)	0.01 (0.01)
	Std error										
1	0.97 (0.04)	0.97 (0.05)	0.72 (0.03)	0.72 (0.06)	0.68 (0.05)	0.69 (0.03)	0.67 (0.01)	0.62 (0.03)	0.68 (0.02)	0.69 (0.05)	0.60 (0.02)
2	0.89 (0.02)	0.88 (0.04)	0.69 (0.01)	0.68 (0.02)	0.63 (0.02)	0.69 (0.02)	0.68 (0.02)	0.61 (0.02)	0.69 (0.01)	0.68 (0.01)	0.62 (0.03)
3	0.87 (0.02)	0.82 (0.04)	0.67 (0.02)	0.68 (0.02)	0.62 (0.02)	0.69 (0.02)	0.68 (0.02)	0.61 (0.02)	0.69 (0.02)	0.67 (0.02)	0.60 (0.01)
	Mean absolute error										
1	0.32 (0.01)	0.30 (0.01)	0.26 (0.00)	0.26 (0.01)	0.25 (0.01)	0.26 (0.01)	0.25 (0.01)	0.24 (0.01)	0.26 (0.00)	0.26 (0.01)	0.24 (0.01)
2	0.30 (0.01)	0.28 (0.01)	0.25 (0.00)	0.25 (0.01)	0.23 (0.00)	0.26 (0.00)	0.26 (0.01)	0.23 (0.00)	0.26 (0.00)	0.25 (0.00)	0.23 (0.01)
3	0.29 (0.00)	0.26 (0.00)	0.25 (0.00)	0.25 (0.00)	0.23 (0.00)	0.25 (0.00)	0.25 (0.00)	0.23 (0.00)	0.26 (0.00)	0.25 (0.00)	0.23 (0.00)
	Mean absolute error 90%										
1	0.19 (0.00)	0.17 (0.00)	0.17 (0.00)	0.17 (0.00)	0.16 (0.00)	0.17 (0.01)	0.16 (0.00)	0.15 (0.00)	0.17 (0.00)	0.17 (0.00)	0.15 (0.00)
2	0.19 (0.00)	0.17 (0.00)	0.17 (0.00)	0.17 (0.00)	0.15 (0.00)	0.17 (0.00)	0.16 (0.00)	0.14 (0.00)	0.16 (0.00)	0.16 (0.00)	0.15 (0.00)
3	0.18 (0.00)	0.16 (0.00)	0.17 (0.00)	0.17 (0.00)	0.15 (0.00)	0.16 (0.00)	0.16 (0.00)	0.14 (0.00)	0.16 (0.00)	0.16 (0.00)	0.14 (0.00)
	Mean squared error										
1	0.95 (0.09)	0.93 (0.10)	0.52 (0.05)	0.53 (0.09)	0.47 (0.07)	0.48 (0.04)	0.45 (0.02)	0.39 (0.04)	0.46 (0.03)	0.48 (0.07)	0.37 (0.02)
2	0.80 (0.04)	0.77 (0.07)	0.48 (0.01)	0.47 (0.03)	0.39 (0.02)	0.48 (0.03)	0.47 (0.03)	0.38 (0.03)	0.47 (0.02)	0.46 (0.02)	0.39 (0.03)
3	0.76 (0.04)	0.67 (0.06)	0.46 (0.02)	0.46 (0.03)	0.39 (0.02)	0.47 (0.02)	0.46 (0.02)	0.37 (0.02)	0.48 (0.02)	0.46 (0.03)	0.35 (0.02)
	R^2										
1	0.87 (0.01)	0.88 (0.01)	0.93 (0.01)	0.93 (0.01)	0.94 (0.01)	0.94 (0.01)	0.94 (0.00)	0.95 (0.01)	0.94 (0.00)	0.94 (0.01)	0.95 (0.00)
2	0.89 (0.01)	0.90 (0.01)	0.94 (0.00)	0.94 (0.00)	0.95 (0.00)	0.94 (0.00)	0.94 (0.00)	0.95 (0.00)	0.94 (0.00)	0.94 (0.00)	0.95 (0.00)
3	0.90 (0.00)	0.91 (0.01)	0.94 (0.00)	0.94 (0.00)	0.95 (0.00)	0.94 (0.00)	0.94 (0.00)	0.95 (0.00)	0.94 (0.00)	0.94 (0.00)	0.95 (0.00)

Table 7
Results for machine learning approaches for prediction of FFR vs. FFR_{3D}. The values represent the averages of the metrics across the 10 random training splits. The bias, error standard deviation and mean absolute errors were calculated based on the quantity $FFR_{3D} - FFR_{NN}$, where FFR_{NN} represent predictions based on the NN approaches. The accuracy, sensitivity and specificity were calculated based on dichotomized data ($FFR_{3D} < 0.8$).

Training-size	$\Delta P_{NN,\Delta P}(X)$		$\Delta P_{NN,\epsilon_{\Delta P}}(X)$			$\Delta P_{NN,\Delta P}(X^{0D})$			$\Delta P_{NN,\epsilon_{\Delta P}}(X^{0D})$		
	X_1	X_2	X_1	X_2	X_3	X_1	X_2	X_3	X_1	X_2	X_3
	Bias										
1	−0.004	−0.005	−0.006	−0.006	−0.002	−0.007	−0.007	−0.003	−0.007	−0.006	−0.003
2	−0.004	−0.005	−0.007	−0.006	−0.004	−0.008	−0.007	−0.004	−0.007	−0.007	−0.004
3	−0.003	−0.005	−0.006	−0.006	−0.005	−0.008	−0.008	−0.004	−0.008	−0.007	−0.005
	Std error										
1	0.030	0.035	0.023	0.024	0.022	0.023	0.023	0.022	0.022	0.023	0.022
2	0.026	0.025	0.022	0.022	0.022	0.022	0.022	0.022	0.022	0.021	0.021
3	0.024	0.023	0.021	0.022	0.022	0.021	0.021	0.021	0.021	0.021	0.021
	Mean absolute error										
1	0.021	0.022	0.018	0.018	0.016	0.018	0.018	0.016	0.018	0.017	0.016
2	0.019	0.018	0.017	0.017	0.017	0.017	0.017	0.016	0.017	0.017	0.016
3	0.018	0.017	0.017	0.017	0.016	0.017	0.017	0.016	0.017	0.017	0.016
	Accuracy										
1	95.533	95.467	95.600	96.533	95.133	96.400	96.667	96.533	96.267	97.000	96.133
2	95.533	96.533	96.067	96.800	95.733	96.533	97.133	96.400	97.067	96.800	96.200
3	95.267	96.067	95.533	96.933	96.400	96.533	97.400	97.267	96.200	97.000	96.600
	Sensitivity										
1	92.333	92.333	93.333	93.333	93.333	90.000	91.333	92.667	89.333	92.000	93.333
2	93.333	92.333	91.667	93.333	92.667	89.333	92.333	92.333	91.667	90.333	91.667
3	94.000	93.000	92.000	92.333	93.333	88.333	91.000	92.000	87.667	89.667	91.667
	Specificity										
1	96.333	96.250	96.167	97.333	95.583	98.000	98.000	97.500	98.000	98.250	96.833
2	96.083	97.583	97.167	97.667	96.500	98.333	98.333	97.417	98.417	98.417	97.333
3	95.583	96.833	96.417	98.083	97.167	98.583	99.000	98.583	98.333	98.833	97.833

A.2. Relative importance of pressure drop according to segment type

The centerlines were divided into healthy sections, stenotic sections and junction regions based on deviations of the locally observed radius from the expected healthy radius of a smoothly tapering vessel predicted as described previously [22,33]. The 3D iNS pressure data from hyperemic simulations from the coronary inlet to the point of measurement location was considered. In this context, $P_{inlet} - P_{distal}$ represents the total pressure drop from the inlet to the point of measurement, and $\sum \Delta P_{segment}$ represents the cumulative pressure drop of all segments of a certain segment type (stenotic, healthy or junction) along the same path, such that:

$$\sum \Delta P_{stenotic} + \sum \Delta P_{healthy} + \sum \Delta P_{junction} = P_{inlet} - P_{distal}\,. \tag{10}$$

As such, Fig. A.1 shows the relative contribution to the total pressure loss for each segment type, plotted vs. FFR_{3D}. The data is represented as a scatter plot, and a second order polynomial function was fitted to the data for each segment type and is also indicated (solid lines). The shaded region represents the 95% confidence interval for the fitted lines.

Table 8
Results for machine learning approaches for prediction of FFR vs. FFR_{meas}. The values represent the averages of the metrics across the 10 random training splits. The bias, error standard deviation and mean absolute errors were calculated based on the quantity $FFR_{meas} - FFR_{NN}$, where FFR_{NN} represent predictions based on the NN approaches. The accuracy, sensitivity and specificity were calculated based on dichotomized data ($FFR_{meas} < 0.8$).

Training-size	$\Delta P_{NN,\Delta P}(X)$		$\Delta P_{NN,\epsilon_{\Delta P}}(X)$			$\Delta P_{NN,\Delta P}(X^{0D})$			$\Delta P_{NN,\epsilon_{\Delta P}}(X^{0D})$		
	X_1	X_2	X_1	X_2	X_3	X_1	X_2	X_3	X_1	X_2	X_3
	Bias										
1	0.017	0.018	0.014	0.016	0.020	0.013	0.014	0.018	0.013	0.015	0.019
2	0.017	0.017	0.014	0.015	0.018	0.013	0.014	0.016	0.013	0.014	0.018
3	0.018	0.016	0.015	0.015	0.017	0.013	0.013	0.017	0.013	0.014	0.017
	Std error										
1	0.125	0.118	0.127	0.127	0.128	0.128	0.129	0.129	0.129	0.130	0.129
2	0.125	0.127	0.128	0.129	0.128	0.130	0.129	0.128	0.130	0.130	0.129
3	0.126	0.127	0.129	0.128	0.127	0.130	0.130	0.129	0.131	0.130	0.129
	Mean absolute error										
1	0.080	0.076	0.078	0.077	0.079	0.077	0.076	0.077	0.078	0.077	0.077
2	0.078	0.078	0.078	0.078	0.078	0.078	0.077	0.077	0.079	0.077	0.078
3	0.078	0.078	0.078	0.077	0.078	0.079	0.077	0.077	0.079	0.077	0.078
	Accuracy										
1	81.400	82.600	83.600	82.400	82.000	82.200	82.600	82.000	82.400	82.600	82.000
2	82.000	82.400	82.400	82.600	82.200	83.400	82.600	82.000	83.200	82.800	82.000
3	82.200	83.000	82.200	82.800	82.000	83.200	82.200	82.000	83.000	82.400	82.000
	Sensitivity										
1	83.077	84.615	83.846	84.615	84.615	80.000	83.077	84.615	83.077	84.615	84.615
2	83.846	83.846	83.846	84.615	84.615	83.846	84.615	84.615	83.077	84.615	84.615
3	83.846	84.615	84.615	84.615	84.615	81.538	84.615	84.615	82.308	84.615	84.615
	Specificity										
1	80.811	81.892	83.514	81.622	81.081	82.973	82.432	81.081	82.162	81.892	81.081
2	81.351	81.892	81.892	81.892	81.351	83.243	81.892	81.081	83.243	82.162	81.081
3	81.622	82.432	81.351	82.162	81.081	83.784	81.351	81.081	83.243	81.622	81.081

A.3. Performance on test and training sets

The mean absolute error and mean squared error for the prediction of pressure drop across stenotic and healthy segments are presented in Fig. A.2. In contrast to the values reported in the main manuscript where the NNs were evaluated on the test set only (solid lines), here we have also included error metrics for the evaluation of the NNs on the learning sets (dashed lines).

A.4. Principal component analysis of radius data

For each segment, the cross-sections were extracted corresponding to each centerline point using VMTK [31], as visualized in Fig. A.3. The cross-sectional area was used to calculate the radius of an equivalent axisymmetric cross-section, r for each centerline point. The minimum and maximum diameter (d_{min} and $d_{\max}$) for each centerline point was extracted and converted to minimum and maximum radius values by division of a factor of two. The radius data for each segment was then re-sampled using 100 points to produce the vectors

$$\vec{r} = \left[r_1, r_2 \dots r_{99}, r_{100}\right] \frac{1}{r_1} \tag{11a}$$

$$\vec{ec} = \left[\frac{d_{min}}{d_{\max\,1}}, \frac{d_{min}}{d_{\max\,2}} \cdots \frac{d_{min}}{d_{\max\,99}}, \frac{d_{min}}{d_{\max\,100}}\right], \tag{11b}$$

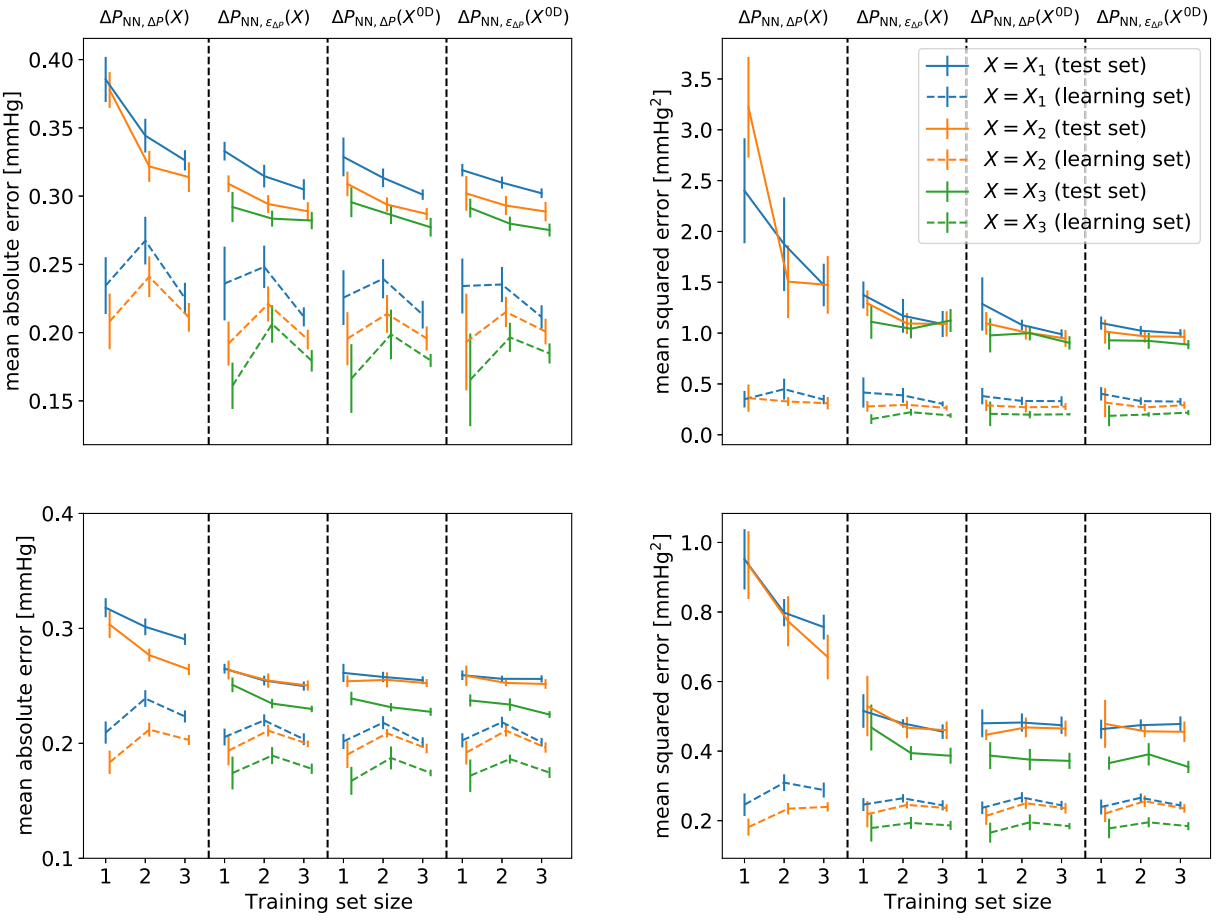

Fig. A.2. Error metrics for the NN models for prediction of pressure losses across stenotic segments (top) and healthy segments (bottom) reported in terms of the mean absolute error and mean squared error. The error metrics are reported for both the test set (solid lines) and the learning sets (dashed lines).

where $\vec{r}$ represent a radius vector and $\vec{ec}$ an eccentricity vector. For simplicity we consider a vector of observations (*i.e.* either $\vec{ec}$ or $\vec{r}$) and denote it $\vec{x}$. All coronary segments (performed individually for stenotic and healthy segments) were then considered and a matrix of row vector observations was assembled:

$$\vec{X} = \begin{bmatrix} \vec{x}^1 \\ \vdots \\ \vec{x}^N \end{bmatrix} . \tag{12}$$

The matrix of observations was then normalized by subtracting the columns mean and a principal component analysis was performed for both radius and eccentricity [40]. The PCA transforms the data onto a new coordinate system for which the first axis explains the maximum amount of information (variation) in the data. All axes are orthogonal and the remaining axis explains decreasing amount of information/variation.

For each training set and validation split considered in this study, the learning data was used to generate the PCA transformation. This transformation was then used to project the vector of observations onto the principal axis/component, and the value/score along the first axis, was extracted for the radius and eccentricity data, *i.e.* $PCA_{r,1}$, $PCA_{ec,1}$.

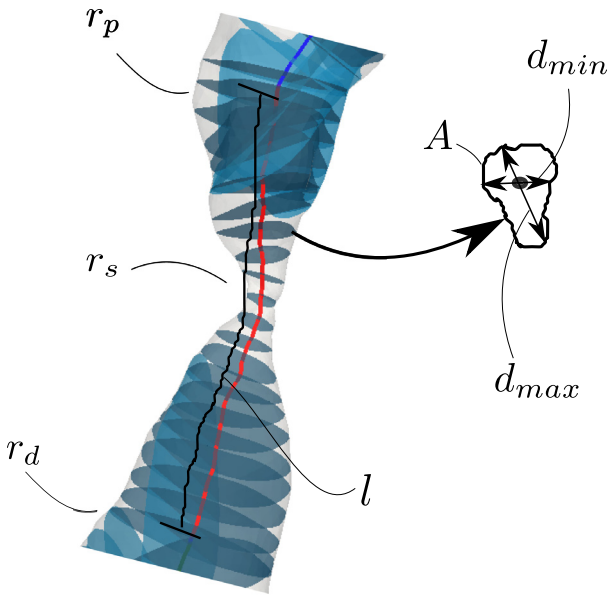

Fig. A.3. Extraction of cross-sections and relevant geometrical data along the centerline of a stenotic segment.

References

[1] B.L. Nørgaard, C.J. Terkelsen, O.N. Mathiassen, E.L. Grove, et al., Coronary CT angiographic and flow reserve-guided management of patients with stable ischemic heart disease, J. Am. Coll. Cardiol. 72 (18) (2018) 2123–2134, http://dx.doi.org/10.1016/j.jacc.2018.07.043, URL http://www.onlinejacc.org/content/72/18/2123.

[2] C. Krittanawong, H. Zhang, Z. Wang, M. Aydar, T. Kitai, Artificial intelligence in precision cardiovascular medicine, J. Am. Coll. Cardiol. 69 (21) (2017) 2657–2664, http://dx.doi.org/10.1016/j.jacc.2017.03.571, URL http://www.sciencedirect.com/science/article/pii/S0735109717368456.

[3] D. Dey, P.J. Slomka, P. Leeson, D. Comaniciu, S. Shrestha, P.P. Sengupta, T.H. Marwick, Artificial intelligence in cardiovascular imaging: JACC state-of-the-art review, J. Am. Coll. Cardiol. 73 (11) (2019) 1317–1335, http://dx.doi.org/10.1016/j.jacc.2018.12.054, Publisher: Journal of the American College of Cardiology Section: The Present and Future. URL http://www.onlinejacc.org/content/73/11/1317.

[4] G. Litjens, F. Ciompi, J.M. Wolterink, B.D. de Vos, T. Leiner, J. Teuwen, I. Išgum, State-of-the-art deep learning in cardiovascular image analysis, JACC: Cardiovasc. Imaging 12 (8, Part 1) (2019) 1549–1565, http://dx.doi.org/10.1016/j.jcmg.2019.06.009, URL http://www.sciencedirect.com/science/article/pii/S1936878X19305753.

[5] A.-V. Bharath, Y. Xiaoying, C.O. Wu, L. Kiang, H.W. Gregory, M. Robyn, S. Gomes Antoinette, R. Folsom Aaron, S. Steven, G. Eliseo, A. Bluemke David, A.C. Lima João, Cardiovascular event prediction by machine learning, Circ. Res. 121 (9) (2017) 1092–1101, http://dx.doi.org/10.1161/CIRCRESAHA.117.311312, Publisher: American Heart Association. URL https://www.ahajournals.org/doi/full/10.1161/CIRCRESAHA.117.311312.

[6] M. Motwani, D. Dey, D.S. Berman, G. Germano, S. Achenbach, M.H. Al-Mallah, D. Andreini, M.J. Budoff, F. Cademartiri, T.Q. Callister, H.-J. Chang, K. Chinnaiyan, B.J.W. Chow, R.C. Cury, A. Delago, M. Gomez, H. Gransar, M. Hadamitzky, J. Hausleiter, N. Hindoyan, G. Feuchtner, P.A. Kaufmann, Y.-J. Kim, J. Leipsic, F.Y. Lin, E. Maffei, H. Marques, G. Pontone, G. Raff, R. Rubinshtein, L.J. Shaw, J. Stehli, T.C. Villines, A. Dunning, J.K. Min, P.J. Slomka, Machine learning for prediction of all-cause mortality in patients with suspected coronary artery disease: a 5-year multicentre prospective registry analysis, Eur. Heart J. 38 (7) (2017) 500–507, http://dx.doi.org/10.1093/eurheartj/ehw188.

[7] L. von Rueden, S. Mayer, K. Beckh, B. Georgiev, S. Giesselbach, R. Heese, B. Kirsch, J. Pfrommer, A. Pick, R. Ramamurthy, M. Walczak, J. Garcke, C. Bauckhage, J. Schuecker, Informed machine learning – A taxonomy and survey of integrating knowledge into learning systems, 2020, arXiv:1903.12394 [cs, stat]. arXiv:1903.12394. URL http://arxiv.org/abs/1903.12394.

[8] M. Raissi, P. Perdikaris, G.E. Karniadakis, Physics-informed neural networks: A deep learning framework for solving forward and inverse problems involving nonlinear partial differential equations, J. Comput. Phys. 378 (2019) 686–707, http://dx.doi.org/10.1016/j.jcp.2018.10.045, URL http://www.sciencedirect.com/science/article/pii/S0021999118307125.

[9] S. Sankaran, L. Grady, C.A. Taylor, Impact of geometric uncertainty on hemodynamic simulations using machine learning, Comput. Methods Appl. Mech. Engrg. 297 (2015) 167–190, http://dx.doi.org/10.1016/j.cma.2015.08.014, URL http://www.sciencedirect.com/science/article/pii/S0045782515002728.

[10] S. Sankaran, L. Grady, C.A. Taylor, Fast computation of hemodynamic sensitivity to lumen segmentation uncertainty, IEEE Trans. Med. Imaging 34 (12) (2015) 2562–2571, http://dx.doi.org/10.1109/TMI.2015.2445777.

[11] A. Karpatne, W. Watkins, J. Read, V. Kumar, Physics-guided neural networks (PGNN): An application in lake temperature modeling, 2018, arXiv:1710.11431 [physics, stat]. arXiv:1710.11431. URL http://arxiv.org/abs/1710.11431.

[12] F. Joly, G. Soulez, S. Lessard, C. Kauffmann, I. Vignon-Clementel, A cohort longitudinal study identifies morphology and hemodynamics predictors of abdominal aortic aneurysm growth, Ann. Biomed. Eng. 48 (2) (2020) 606–623, http://dx.doi.org/10.1007/s10439-019-02375-1.

[13] G. Kissas, Y. Yang, E. Hwuang, W.R. Witschey, J.A. Detre, P. Perdikaris, Machine learning in cardiovascular flows modeling: Predicting arterial blood pressure from non-invasive 4D flow MRI data using physics-informed neural networks, Comput. Methods Appl. Mech. Engrg. 358 (2020) 112623, http://dx.doi.org/10.1016/j.cma.2019.112623, URL http://www.sciencedirect.com/science/article/pii/S0045782519305055.

[14] ESC guidelines for the diagnosis and management of chronic coronary syndromes, Eur. Heart J. (2019) Oxford Academic. URL https://academic.oup.com/eurheartj/article/41/3/407/5556137.

[15] B. Hannawi, W.W. Lam, S. Wang, G.A. Younis, Current use of fractional flow reserve: a nationwide survey, Texas Heart Inst. J. 41 (6) (2014) 579–584, http://dx.doi.org/10.14503/THIJ-13-3917.

[16] C.A. Taylor, T.A. Fonte, J.K. Min, Computational fluid dynamics applied to cardiac computed tomography for noninvasive quantification of fractional flow reserve, J. Am. Coll. Cardiol. 61 (22) (2013) 2233–2241, http://dx.doi.org/10.1016/j.jacc.2012.11.083, URL http://linkinghub.elsevier.com/retrieve/pii/S0735109713013041.

[17] P.D. Morris, D. Ryan, A.C. Morton, R. Lycett, P.V. Lawford, D.R. Hose, J.P. Gunn, Virtual fractional flow reserve from coronary angiography: Modeling the significance of coronary lesions, JACC: Cardiovas. Interv. 6 (2) (2013) 149–157, http://dx.doi.org/10.1016/j.jcin.2012.08.024, URL http://linkinghub.elsevier.com/retrieve/pii/S1936879812011673.

[18] S. Tu, E. Barbato, Z. Köszegi, J. Yang, Z. Sun, N.R. Holm, B. Tar, Y. Li, D. Rusinaru, W. Wijns, J.H. Reiber, Fractional flow reserve calculation from 3-dimensional quantitative coronary angiography and TIMI frame count, JACC: Cardiovas. Interv. 7 (7) (2014) 768–777, http://dx.doi.org/10.1016/j.jcin.2014.03.004, URL http://linkinghub.elsevier.com/retrieve/pii/S1936879814007912.

[19] L. Itu, P. Sharma, V. Mihalef, A. Kamen, C. Suciu, D. Lomaniciu, A patient-specific reduced-order model for coronary circulation, in: 2012 9th IEEE International Symposium on Biomedical Imaging (ISBI), IEEE, 2012, pp. 832–835, URL http://ieeexplore.ieee.org/xpls/abs_all.jsp?arnumber=6235677.

[20] P.J. Blanco, C.A. Bulant, L.O. Müller, G.D.M. Talou, C.G. Bezerra, P.L. Lemos, R.A. Feijóo, Comparison of 1D and 3D models for the estimation of fractional flow reserve, Sci. Rep. 8 (1) (2018) http://dx.doi.org/10.1038/s41598-018-35344-0, URL http://www.nature.com/articles/s41598-018-35344-0.

[21] E. Boileau, S. Pant, C. Roobottom, I. Sazonov, J. Deng, X. Xie, P. Nithiarasu, Estimating the accuracy of a reduced-order model for the calculation of fractional flow reserve (FFR), Int. J. Numer. Methods Biomed. Eng. 34 (1) (2018) e2908, http://dx.doi.org/10.1002/cnm.2908, URL http://doi.wiley.com/10.1002/cnm.2908.

[22] F.E. Fossan, J. Sturdy, L.O. Müller, A. Strand, A.T. Bråten, A. Jrgensen, R. Wiseth, L.R. Hellevik, Uncertainty quantification and sensitivity analysis for computational FFR estimation in stable coronary artery disease, Cardiovas. Eng. Technol. (2018) http://dx.doi.org/10.1007/s13239-018-00388-w, URL http://link.springer.com/10.1007/s13239-018-00388-w.

[23] M. Zreik, N. Lessmann, R.W. van Hamersvelt, J.M. Wolterink, M. Voskuil, M.A. Viergever, T. Leiner, I. Išgum, Deep learning analysis of the myocardium in coronary CT angiography for identification of patients with functionally significant coronary artery stenosis, Med. Image Anal. 44 (2018) 72–85, http://dx.doi.org/10.1016/j.media.2017.11.008.

[24] H. Hae, S.-J. Kang, W.-J. Kim, S.-Y. Choi, J.-G. Lee, Y. Bae, H. Cho, D.H. Yang, J.-W. Kang, T.-H. Lim, C.H. Lee, D.-Y. Kang, P.H. Lee, J.-M. Ahn, D.-W. Park, S.-W. Lee, Y.-H. Kim, C.W. Lee, S.-W. Park, S.-J. Park, Machine learning assessment of myocardial ischemia using angiography: Development and retrospective validation, PLOS Med. 15 (11) (2018) e1002693, http://dx.doi.org/10.1371/journal.pmed.1002693, URL https://journals.plos.org/plosmedicine/article?id=10.1371/journal.pmed.1002693.

[25] D. Dey, S. Gaur, K.A. Ovrehus, P.J. Slomka, J. Betancur, M. Goeller, M.M. Hell, H. Gransar, D.S. Berman, S. Achenbach, H.E. Botker, J.M. Jensen, J.F. Lassen, B.L. Norgaard, Integrated prediction of lesion-specific ischaemia from quantitative coronary CT angiography using machine learning: a multicentre study, Eur. Radiol. 28 (6) (2018) 2655–2664, http://dx.doi.org/10.1007/s00330-017-5223-z.

[26] K.K. Kumamaru, S. Fujimoto, Y. Otsuka, T. Kawasaki, Y. Kawaguchi, E. Kato, K. Takamura, C. Aoshima, Y. Kamo, Y. Kogure, H. Inage, H. Daida, S. Aoki, Diagnostic accuracy of 3D deep-learning-based fully automated estimation of patient-level minimum fractional flow reserve from coronary computed tomography angiography, Eur. Heart J. Cardiovas. Imaging (2019) http://dx.doi.org/10.1093/ehjci/jez160.

[27] L. Itu, S. Rapaka, T. Passerini, B. Georgescu, C. Schwemmer, M. Schoebinger, T. Flohr, P. Sharma, D. Comaniciu, A machine-learning approach for computation of fractional flow reserve from coronary computed tomography, J. Appl. Physiol. 121 (1) (2016) 42–52, http://dx.doi.org/10.1152/japplphysiol.00752.2015, URL http://jap.physiology.org/lookup/doi/10.1152/japplphysiol.00752.2015.

[28] A.T. Bråten, R. Wiseth, Diagnostic accuracy of CT-FFR compared to invasive coronar angiography with fractional flow reserve - full text view - clinicaltrials.gov, 2017, URL https://clinicaltrials.gov/ct2/show/NCT03045601.

[29] L.O. Müller, F.E. Fossan, A.T. Bråten, A. Jørgensen, R. Wiseth, L.R. Hellevik, Impact of baseline coronary flow and its distribution on fractional flow reserve prediction, Int. J. Numer. Methods Biomed. Eng. n/a (n/a) (2019) e3246, http://dx.doi.org/10.1002/cnm.3246, URL https://onlinelibrary.wiley.com/doi/abs/10.1002/cnm.3246.

[30] P.A. Yushkevich, J. Piven, H.C. Hazlett, R.G. Smith, S. Ho, J.C. Gee, G. Gerig, User-guided 3D active contour segmentation of anatomical structures: Significantly improved efficiency and reliability, NeuroImage 31 (3) (2006) 1116–1128, http://dx.doi.org/10.1016/j.neuroimage.2006.01.015, URL http://linkinghub.elsevier.com/retrieve/pii/S1053811906000632.

[31] L. Antiga, M. Piccinelli, L. Botti, B. Ene-Iordache, A. Remuzzi, D.A. Steinman, An image-based modeling framework for patient-specific computational hemodynamics, Med. Biol. Eng. Comput. 46 (11) (2008) 1097–1112, http://dx.doi.org/10.1007/s11517-008-0420-1, URL http://link.springer.com/10.1007/s11517-008-0420-1.

[32] O. srl, The vascular modeling toolkit website, 2017, Accessed: 2017-10-27. URL https://www.vmtk.org.
[33] R. Shahzad, H. Kirili, C. Metz, H. Tang, M. Schaap, L. van Vliet, W. Niessen, T. van Walsum, Automatic segmentation, detection and quantification of coronary artery stenoses on CTA, Int. J. Cardiovas. Imaging 29 (8) (2013) 1847–1859, http://dx.doi.org/10.1007/s10554-013-0271-1, bibtex[pmid=23925713].
[34] R.F. Wilson, K. Wyche, B.V. Christensen, S. Zimmer, D.D. Laxson, Effects of adenosine on human coronary arterial circulation, Circulation 82 (5) (1990) 1595–1606, http://dx.doi.org/10.1161/01.CIR.82.5.1595, URL http://circ.ahajournals.org/content/82/5/1595.
[35] A. Logg, K.-A. Mardal, G. Wells (Eds.), Automated Solution of Differential Equations by the Finite Element Method, in: Lecture Notes in Computational Science and Engineering, vol. 84, Springer Berlin Heidelberg, Berlin, Heidelberg, 2012, http://dx.doi.org/10.1007/978-3-642-23099-8, URL http://link.springer.com/10.1007/978-3-642-23099-8.
[36] Ø. Evju, M.S. Alnæs, CBCFLOW, in: Bitbucket Repository, 2017.
[37] H.Y. Kim, H.-S. Lim, J.-H. Doh, C.-W. Nam, E.-S. Shin, B.-K. Koo, M.-H. Yoon, S.-J. Tahk, D.K. Kang, Y.B. Song, J.-Y. Hahn, S.H. Choi, H.-C. Gwon, S.-H. Lee, E.-K. Kim, S.M. Kim, Y. Choe, J.-H. Choi, Physiological severity of coronary artery stenosis depends on the amount of myocardial mass subtended by the coronary artery, JACC. Cardiovas. Interv. 9 (15) (2016) 1548–1560, http://dx.doi.org/10.1016/j.jcin.2016.04.008.
[38] B.D. Seeley, D.F. Young, Effect of geometry on pressure losses across models of arterial stenoses, J. Biomech. 9 (7) (1976) 439–448, http://dx.doi.org/10.1016/0021-9290(76)90086-5, URL http://www.sciencedirect.com/science/article/pii/0021929076900865.
[39] M. Mirramezani, S.L. Diamond, H.I. Litt, S.C. Shadden, Reduced order models for transstenotic pressure drop in the coronary arteries, J. Biomech. Eng. 141 (3) (2019) http://dx.doi.org/10.1115/1.4042184, Publisher: American Society of Mechanical Engineers Digital Collection. URL https://asmedigitalcollection.asme.org/biomechanical/article/141/3/031005/367525/Reduced-Order-Models-for-Transstenotic-Pressure.
[40] H. Abdi, L.J. Williams, Principal component analysis, WIREs Comput. Stat. 2 (4) (2010) 433–459, http://dx.doi.org/10.1002/wics.101, _eprint: https://onlinelibrary.wiley.com/doi/pdf/10.1002/wics.101. URL https://onlinelibrary.wiley.com/doi/abs/10.1002/wics.101.
[41] F. Chollet, et al., Keras, 2020, URL https://keras.io.
[42] M. Abadi, et al., TensorFlow: Large-scale machine learning on heterogeneous systems, 2020, URL https://www.tensorflow.org/.
[43] D.P. Kingma, J. Ba, Adam: A method for stochastic optimization, 2017, arXiv:1412.6980 [cs]. arXiv:1412.6980. URL http://arxiv.org/abs/1412.6980.
[44] S. Russel, P. Norvig, Artificial Intelligence: A Modern Approach (3rd Edition), third ed., Prentice Hall, 2009.
[45] N.P. Johnson, D.T. Johnson, R.L. Kirkeeide, C. Berry, B. De Bruyne, W.F. Fearon, K.G. Oldroyd, N.H.J. Pijls, K.L. Gould, Repeatability of fractional flow reserve despite variations in systemic and coronary hemodynamics, JACC: Cardiovas. Interv. 8 (8) (2015) 1018–1027, http://dx.doi.org/10.1016/j.jcin.2015.01.039, URL http://www.sciencedirect.com/science/article/pii/S1936879815006998.
[46] M. Raissi, P. Perdikaris, G.E. Karniadakis, Physics informed deep learning (Part I): Data-driven solutions of nonlinear partial differential equations, 2017, arXiv:1711.10561 [cs, math, stat]. arXiv:1711.10561. URL http://arxiv.org/abs/1711.10561.
[47] F. Regazzoni, L. Dedè, A. Quarteroni, Machine learning of multiscale active force generation models for the efficient simulation of cardiac electromechanics, Comput. Methods Appl. Mech. Engrg. 370 (2020) 113268, http://dx.doi.org/10.1016/j.cma.2020.113268, URL http://www.sciencedirect.com/science/article/pii/S0045782520304539.
[48] Y. Huo, M. Svendsen, J.S. Choy, Z.-D. Zhang, G.S. Kassab, A validated predictive model of coronary fractional flow reserve, J. R. Soc. Interface 9 (71) (2012) 1325–1338, http://dx.doi.org/10.1098/rsif.2011.0605, URL https://www.ncbi.nlm.nih.gov/pmc/articles/PMC3350723/.
[49] B. Meier, A.R. Gruentzig, J. Hollman, T. Ischinger, J.M. Bradford, Does length or eccentricity of coronary stenoses influence the outcome of transluminal dilatation? Circulation 67 (3) (1983) 497–499, http://dx.doi.org/10.1161/01.CIR.67.3.497, Publisher: American Heart Association. URL https://www.ahajournals.org/doi/10.1161/01.CIR.67.3.497.
[50] C. Pagiatakis, J.-C. Tardif, P.L. L'Allier, R. Mongrain, Effect of stenosis eccentricity on the functionality of coronary bifurcation lesions—a numerical study, Med. Biol. Eng. Comput. 55 (12) (2017) 2079–2095, http://dx.doi.org/10.1007/s11517-017-1653-7.
[51] L. Liang, W. Mao, W. Sun, A feasibility study of deep learning for predicting hemodynamics of human thoracic aorta, J. Biomech. 99 (2020) 109544, http://dx.doi.org/10.1016/j.jbiomech.2019.109544, URL http://www.sciencedirect.com/science/article/pii/S0021929019308012.
[52] R.C. Gosling, J. Sturdy, P.D. Morris, F.E. Fossan, L.R. Hellevik, P. Lawford, D.R. Hose, J. Gunn, Effect of side branch flow upon physiological indices in coronary artery disease, J. Biomech. 103 (2020) 109698, http://dx.doi.org/10.1016/j.jbiomech.2020.109698, URL http://www.sciencedirect.com/science/article/pii/S0021929020301147.
[53] J. Kim, D. Jin, H. Choi, J. Kweon, D.H. Yang, Y.-H. Kim, A zero-dimensional predictive model for the pressure drop in the stenotic coronary artery based on its geometric characteristics, J. Biomech. 113 (2020) 110076, http://dx.doi.org/10.1016/j.jbiomech.2020.110076, URL http://www.sciencedirect.com/science/article/pii/S0021929020305005.
[54] M. Mirramezani, S.C. Shadden, A distributed lumped parameter model of blood flow, Ann. Biomed. Eng. 48 (12) (2020) 2870–2886, http://dx.doi.org/10.1007/s10439-020-02545-6.
[55] Y. Bengio, P. Simard, P. Frasconi, Learning long-term dependencies with gradient descent is difficult, IEEE Trans. Neural Netw. 5 (2) (1994) 157–166, http://dx.doi.org/10.1109/72.279181, Conference Name: IEEE Transactions on Neural Networks.
[56] S. Hochreiter, J. Schmidhuber, Long short-term memory, Neural Comput. (1997) Publisher: MIT Press PUB1010 Cambridge, MA, USA. URL https://dl.acm.org/doi/abs/10.1162/neco.1997.9.8.1735.